

UCLA

UCLA Previously Published Works

Title

An energy and potential enstrophy conserving numerical scheme for the multi-layer shallow water equations with complete Coriolis force

Permalink

<https://escholarship.org/uc/item/5129g3n1>

Authors

Stewart, Andrew L
Dellar, Paul J

Publication Date

2016-05-01

DOI

10.1016/j.jcp.2015.12.042

Peer reviewed

An energy and potential enstrophy conserving numerical scheme for the multi-layer shallow water equations with complete Coriolis force

Andrew L. Stewart^a, Paul J. Dellar^b

^a*Department of Atmospheric and Oceanic Sciences, University of California, Los Angeles, CA 90095, USA*

^b*OCIAM, Mathematical Institute, Andrew Wiles Building, Radcliffe Observatory Quarter, Woodstock Road, Oxford OX2 6GG, UK*

Abstract

We present an energy- and potential enstrophy-conserving scheme for the non-traditional shallow water equations that include the complete Coriolis force and topography. These integral conservation properties follow from material conservation of potential vorticity in the continuous shallow water equations. The latter property cannot be preserved by a discretisation on a fixed Eulerian grid, but exact conservation of a discrete energy and a discrete potential enstrophy seems to be an effective substitute that prevents any distortion of the forward and inverse cascades in quasi-two dimensional turbulence through spurious sources and sinks of energy and potential enstrophy, and also increases the robustness of the scheme against nonlinear instabilities. We exploit the existing Arakawa–Lamb scheme for the traditional shallow water equations, reformulated by Salmon as a discretisation of the Hamiltonian and Poisson bracket. The non-rotating, traditional, and our non-traditional shallow water equations all share the same continuous Hamiltonian structure and Poisson bracket, provided one distinguishes between the particle velocity and the canonical momentum per unit mass. We have determined a suitable discretisation of the non-traditional canonical momentum, which includes additional coupling between the layer thickness and velocity fields, and modified the discrete kinetic energy to suppress an internal symmetric computational instability that otherwise arises for multiple layers. The resulting scheme exhibits the expected second-order convergence under spatial grid refinement. We also show that the drifts in the discrete total energy and potential enstrophy due to temporal truncation error may be reduced to machine precision under suitable refinement of the timestep using the third-order Adams–Bashforth or fourth-order Runge–Kutta integration schemes.

Keywords:

geophysical fluid dynamics, energy conserving schemes, Hamiltonian structures

1. Introduction

Geophysical fluid dynamics is concerned with the large-scale motions of stratified fluid on a rotating, near-spherical planet. In principle such motions are governed by the compressible Navier–Stokes equations as modified to include rotation, but simplified and approximate forms of these equations are widely used in both theoretical and computational models [1, 2]. At large scales viscous effects are relatively unimportant, and usually neglected. The resulting inviscid equations possess various conservation laws, for instance of energy, momentum, and potential vorticity [2]. The last property is perhaps the most important. Energy and momentum may be transported over large distances by waves, but potential vorticity is tied to fluid elements [3]. It is desirable for the simplified and approximated equations to share these conservation properties, and (as far as possible) for any numerical scheme to preserve them too.

Planetary scale fluid flow is typically dominated by the Coriolis force. However, almost all models of the ocean and atmosphere employ the so-called “traditional approximation” [4]. This retains only the contribution to the Coriolis force from the component of the planetary rotation vector that is locally normal to geopotential surfaces. The traditional approximation is typically justified on the basis that the vertical lengthscales of rotationally-dominated geophysical flows are much smaller than their horizontal lengthscales

[5]. However, the “non-traditional” component of the Coriolis force is dynamically important in a wide range of geophysical flows [6]. In the ocean, nontraditional effects can substantially alter the structure and propagation properties of gyroscopic and internal waves [7, 8, 9, 10, 11, 12], the development and growth rate of inertial instabilities [13, 14], the instability of Ekman layers [15], high-latitude deep convection [16], the static stability of the water column [17], and the flow of abyssal waters close to the equator [18, 19, 20]. A parallel line of development has led to “deep atmosphere” models that include non-traditional effects [21, 22, 23, 24, 25, 26].

The focus of this article is a set of shallow water equations that include the full Coriolis force [27, 28]. Shallow water models approximate the ocean’s stratification using a stack of layers of constant-density fluid. This is equivalent to a Lagrangian vertical discretisation of the water column using density as the vertical coordinate. Density or isopycnal coordinates are a natural choice for ocean models because mixing and transport across isopycnal surfaces in the ocean interior is weak, so large-scale flows are largely constrained to flow along density surfaces [29]. Models based on vertical coordinates aligned with surfaces of constant geopotential tend to produce spuriously large diabatic mixing due to the slight misalignment between grid cells and isopycnal surfaces [30]. Shallow water and isopycnal coordinate models are thus widely used to study the ocean circulation, both in conceptual modelling studies and comprehensive ocean models [31, 32, 33]. This isopycnal modelling framework has recently been extended to solve the non-hydrostatic three-dimensional stratified equations with the non-traditional components of the Coriolis force [34].

In this paper we derive an energy- and potential enstrophy-conserving numerical scheme for our extended shallow water equations that include the complete Coriolis force [27, 28]. There are three principal motivations for exactly preserving these conservation laws in our scheme:

1. Ideally any numerical scheme should materially conserve potential vorticity, as this is a crucial dynamical variable in large-scale geophysical flows [3]. Material conservation of potential vorticity, $Dq/Dt = 0$, implies conservation of all the integral moments of q ,

$$\frac{d}{dt} \int hc(q) \, dx dy = 0, \quad (1)$$

for any function $c(q)$. These spatial integrals are much more amenable to approximation on a fixed grid. The most important is conservation of potential enstrophy, for which $c(q) = q^2$. However, exact material conservation of potential vorticity is only possible via specialised Lagrangian schemes such as the particle-mesh method [35] or the contour-advective semi-Lagrangian method [36]. Thompson [37] showed that a vorticity evolution equation for an incompressible fluid that conserves energy and potential enstrophy, and satisfies reasonable properties such as spatial locality (for the streamfunction) and invariance under rotations, is inevitably of material conservation form. Although derived for partial differential equations in continuous space, this result suggests that conservation of energy and potential enstrophy on a fixed Eulerian grid provides a suitable substitute for material conservation of potential vorticity.

2. Conservation of energy and potential enstrophy is crucial for the development of the simultaneous inverse cascade of energy and forward cascade of potential enstrophy that characterises quasi-two-dimensional turbulence [2]. Long-term integrations using non-conservative finite-difference schemes are prone to a spurious cascade of energy towards the scale of the grid spacing, where the spatial truncation error is largest [38]. Conserving the discrete analogue of total energy alone does not prevent the cascade of energy to small scales, and leads to an increase in potential enstrophy [39]. Thus long-time integrations require a scheme that conserves both energy and potential enstrophy, though even this is not sufficient to completely eliminate spurious spectral transfers of these quantities [40].
3. Enforcing these conservation properties eliminates the possibility of nonlinear instabilities driven by spurious sources of energy or potential enstrophy at the grid scale. For example, Fornberg [41] showed that the only stable member of a class of semi-discrete centred finite difference schemes for the inviscid Burgers equation is the scheme that conserves a discrete energy.

Arakawa [38] constructed a finite difference scheme for the two-dimensional incompressible Euler equations, now known as the “Arakawa Jacobian”, that exactly conserves a discrete kinetic energy and a discrete

enstrophy when formulated in continuous time. Arakawa & Lamb [42] later extended this approach to construct a finite difference scheme for the inviscid shallow water equations that exactly conserves total mass, energy, and potential enstrophy. The spurious energy cascades observed in non-conservative long-time integrations of the SWE (see point 2 above) are due to errors introduced in the spatial, rather than temporal, discretisation [39], as we shall confirm in §5. The Arakawa–Lamb scheme therefore discretises only the spatial derivatives of the traditional shallow water equations, yielding evolution equations in continuous time for the discrete particle velocities and layer thicknesses at spatial grid points. This semi-discrete finite difference scheme has since been extended to multiple layers [43], to fourth-order accuracy for the vorticity in the non-divergent limit [44, 45, 46, 47], to spherical geodesic grids [48], and to unstructured finite element meshes [49].

Arakawa & Lamb [42] began with a general finite difference discretisation of the shallow water equations on a staggered grid, known as the Arakawa C-grid, as sketched in figure 1. They wrote down a discretisation that contained many undetermined coefficients, including some unphysical Coriolis terms that were parallel, not perpendicular, to the fluid velocity. They obtained a scheme that conserves consistent spatially discrete approximations to the energy and potential enstrophy via direct algebraic manipulation of the discrete equations to determine suitable coefficients. In particular, the coefficients of the unphysical Coriolis terms become proportional to grid spacing squared. That a discrete scheme should exist that conserves not quadratic invariants like the Arakawa Jacobian [38], but a cubic quantity (energy) and a quotient (potential enstrophy) was long mysterious.

Salmon [47] interpreted the Arakawa–Lamb scheme as a particular discretisation of a non-canonical Hamiltonian formulation of the traditional shallow water equations, in which the evolution is expressed using a Hamiltonian functional and Poisson bracket. Symmetries of a Hamiltonian system correspond directly to conservation laws via Noether’s theorem, making this a natural starting point for the development of conservative schemes. The equations of ideal fluid mechanics, including the shallow water equations, can be expressed as non-canonical Hamiltonian systems using space-fixed Eulerian variables [50, 2, 51, 52]. To keep the canonical form of Hamilton’s equations one must either use Lagrangian variables that follow fluid elements, or introduce artificial Clebsch potentials.

The non-rotating, traditional, and our non-traditional shallow water equations all share the same Hamiltonian structure and Poisson bracket, provided one distinguishes between the particle velocity and the canonical momentum per unit mass [27, 28]. This distinction is often glossed over in the traditional shallow water equations because the two differ only by a function of space alone, so their time derivatives are identical. We use this insight to construct an analog of the Arakawa–Lamb scheme for our non-traditional shallow water equations by adapting Salmon’s [47] Hamiltonian formulation. The main difficulty we encounter is that the layer thickness field enters the canonical momentum through the non-traditional terms, so we need to find a suitable average of the layer thickness field that is compatible with the placement of variables on the Arakawa C grid. Like the Arakawa Jacobian and Arakawa–Lamb schemes, we obtain a system of ordinary differential equations (ODEs) for the evolution in time of field values at grid points. Discrete analogs of the energy \mathcal{E} and potential enstrophy \mathcal{P} are exactly conserved under the exact evolution of this ODE system. To get a concrete numerical scheme we further discretise in time using the 4th order Runge–Kutta and 3rd order Adams–Bashforth schemes [53]. We investigate the time step that is necessary to reduce the temporal truncation errors in our discrete approximations of \mathcal{E} and \mathcal{P} down to machine precision.

Recently a similar Hamiltonian and Poisson bracket formulation has been employed to derive energy conserving schemes for the deep and shallow atmosphere equations [54], again using the canonical momenta to formulate the discrete Poisson bracket and ensure antisymmetry. However, these authors were unable to construct a discrete Poisson bracket that conserves potential enstrophy. A more general approach to constructing schemes that conserve energy and potential enstrophy formulates the shallow water equations as evolution equations for the potential vorticity, divergence, and layer thickness fields using discrete Nambu brackets [55, 56]. This formulation requires an elliptic inversion to compute the velocity field, which is computationally expensive but allows for a straightforward incorporation of boundary conditions.

The structure of this paper is as follows. In §2 we briefly review the shallow water equations with complete Coriolis force and their Hamiltonian formulation [27, 28]. In §3 we review Salmon’s Hamiltonian derivation of the Arakawa–Lamb scheme for the traditional shallow water equations (§3.1), and extend it to

include the complete Coriolis force in a single layer (§3.2) and in multiple layers (§3.3). In §4 we present a series of numerical verification experiments, and in §5 we demonstrate that energy and potential enstrophy can be conserved to machine precision if the time-step is sufficiently short. Finally, in §6 we summarise our results and provide concluding remarks.

2. Shallow water equations with complete Coriolis force

The derivation of our numerical scheme begins with the non-canonical Hamiltonian formulation of the traditional shallow water equations, henceforth abbreviated as SWE, as described in [50, 51, 52]. The single and multi-layer non-traditional shallow water equations (henceforth NTSWE) were recently derived in [27, 28]. For clarity we first present the non-canonical Hamiltonian formulation of the single-layer NTSWE.

We begin by writing the single layer NTSWE [27, 28] in the vector invariant form [57],

$$\frac{\partial \tilde{u}}{\partial t} - hqv + \frac{\partial \Phi}{\partial x} = 0, \quad (2a)$$

$$\frac{\partial \tilde{v}}{\partial t} + hqu + \frac{\partial \Phi}{\partial y} = 0, \quad (2b)$$

$$\frac{\partial h}{\partial t} + \frac{\partial}{\partial x}(hu) + \frac{\partial}{\partial y}(hv) = 0. \quad (2c)$$

These equations are written in pseudo-Cartesian coordinates with x and y denoting horizontal distances within a constant geopotential surface [5, 58]. The effective gravity g acts in the z direction perpendicular to this surface. They describe a layer of inviscid fluid flowing over bottom topography at $z = h_b(x, y)$ in a frame rotating with angular velocity vector $\boldsymbol{\Omega} = (\Omega^{(x)}, \Omega^{(y)}, \Omega^{(z)})$. We allow for an arbitrary orientation of the x and y axes with respect to North, so $\Omega^{(x)}$ and $\Omega^{(y)}$ may both be non-zero, and may depend arbitrarily on x and y , but not z [28].

The mass conservation equation (2c) for the fluid layer thickness $h(x, y, t)$ contains the particle velocity components u and v in the x and y directions. These particle velocity components also appear in the Bernoulli potential

$$\Phi = \frac{1}{2}u^2 + \frac{1}{2}v^2 + g(h_b + h) + h \left(\Omega^{(x)}v - \Omega^{(y)}u \right). \quad (3)$$

The vertical momentum equation for the underlying three-dimensional fluid contains additional non-traditional contributions proportional to the horizontal components $\Omega^{(x)}$ and $\Omega^{(y)}$ of the rotation vector. The three-dimensional pressure whose depth-average appears in the shallow water equation thus satisfies a three-dimensional quasihydrostatic balance [22], rather than the usual hydrostatic balance.

However, the time derivatives in (2a) and (2b) are of the canonical velocity components

$$\tilde{u} = u + 2\Omega^{(y)} \left(h_b + \frac{1}{2}h \right), \quad \tilde{v} = v - 2\Omega^{(x)} \left(h_b + \frac{1}{2}h \right), \quad (4)$$

which together form the vector $\tilde{\mathbf{u}} = (\tilde{u}, \tilde{v})$. These velocity components also appear in the potential vorticity

$$q = \frac{1}{h} \left(2\Omega^{(z)} + \frac{\partial \tilde{v}}{\partial x} - \frac{\partial \tilde{u}}{\partial y} \right), \quad (5)$$

where $\Omega^{(z)}$ is the component of the rotation vector parallel to the z -axis.

We call $\tilde{\mathbf{u}}$ the canonical velocity because it is related to the canonical momentum per unit mass, or to the depth-average of the particle velocity relative to an inertial frame [27, 28]. For spatially-uniform $\Omega^{(x)}$, $\Omega^{(y)}$, $\Omega^{(z)}$, *i.e.* making an f -plane approximation, the latter quantity is

$$\tilde{\tilde{u}} = u - \Omega^{(z)}y + 2\Omega^{(y)} \left(h_b + \frac{1}{2}h \right), \quad \tilde{\tilde{v}} = v + \Omega^{(z)}x - 2\Omega^{(x)} \left(h_b + \frac{1}{2}h \right), \quad (6)$$

which may be derived from the depth average of the three-dimensional vector field

$$\tilde{\tilde{\mathbf{u}}} = \mathbf{u} + \boldsymbol{\Omega} \times \mathbf{x} + \nabla(xz\Omega^{(y)} - yz\Omega^{(x)}) = \mathbf{u} + (2z\Omega^{(y)} - y\Omega^{(z)}, x\Omega^{(z)} - 2z\Omega^{(x)}, 0). \quad (7)$$

The first two terms $\mathbf{u} + \boldsymbol{\Omega} \times \mathbf{x}$ give the three-dimensional velocity relative to an inertial frame. The additional gradient of a gauge potential eliminates the vertical component of the vector potential for the Coriolis force, as required for a shallow water system formulated in terms of the depth-averaged horizontal velocity alone.

The potential vorticity is

$$q = \frac{1}{h} \left(\frac{\partial \tilde{v}}{\partial x} - \frac{\partial \tilde{u}}{\partial y} \right), \quad (8)$$

with no explicit contribution from the rotation vector. The terms proportional to $\Omega^{(z)}$ in (6) are independent of time, so they do not contribute to the time derivatives in (2a) and (2b). Thus the distinction between the particle velocity and canonical velocity is commonly not made in the traditional shallow water equations, in which the additional terms proportional to both $\Omega^{(x)}$, $\Omega^{(y)}$ and the time-dependent $h(x, y, t)$ are absent.

Instead, the contribution from $\Omega^{(z)}$ is put explicitly in the definition (5) of the potential vorticity. By using (4) instead of (6) we omit the time-independent terms proportional to $\Omega^{(z)}$, which are much larger than the other terms in the canonical momenta (by a factor of the inverse Rossby number). This reduces the accumulation of floating point round-off errors in transforming between the canonical and particle velocities. It is also then straightforward to impose periodic boundary conditions, because the explicit x and y dependence in (6) is absent. Moreover, the non-traditional numerical scheme we derive below will reduce to the exact form of the Arakawa–Lamb scheme when we set $\Omega^{(x)}$ and $\Omega^{(y)}$ to zero. Conversely, the additional terms proportional to x and y in (6) will be differentiated exactly by a second-order accurate spatial discretisation, so the equivalent scheme based on the full canonical velocity (6) instead of (4) would give identical results in exact arithmetic.

By distinguishing between the particle velocity \mathbf{u} and the canonical velocity $\tilde{\mathbf{u}}$ we have written the NTSWE in the same structural form (2a)–(2c) as the SWE. However, in the following we treat the particle velocity as a known function of the canonical velocity and the layer thickness, as given by solving (4) for $\mathbf{u} = \mathbf{u}(\tilde{\mathbf{u}}, h)$.

The Hamiltonian for the system (2a)–(2c) is simply the total energy, which is independent of the Coriolis force when expressed in terms of the particle velocity components u and v ,

$$\mathcal{H} = \mathcal{E} = \iint d\mathbf{x} \left\{ \frac{1}{2} h (u^2 + v^2) + gh (h_b + \frac{1}{2} h) \right\}. \quad (9)$$

However, we treat $\mathcal{H} = \mathcal{H}[\mathbf{u}(\tilde{\mathbf{u}}, h), h]$ as a functional of the canonical velocity components and layer thickness. We do not specify a domain of integration for this functional, but assume that the boundaries of the domain are periodic, or permit no normal fluxes, to allow us to integrate by parts as necessary below without acquiring boundary terms.

The non-canonical Hamiltonian formalism expresses the time evolution of any functional \mathcal{F} in terms of a Poisson bracket as [50, 2, 51, 52]

$$\frac{d\mathcal{F}}{dt} = \{\mathcal{F}, \mathcal{H}\}. \quad (10)$$

The Poisson bracket must be bilinear, antisymmetric, and satisfy the Jacobi identity

$$\{\mathcal{F}, \{\mathcal{G}, \mathcal{K}\}\} + \{\mathcal{G}, \{\mathcal{K}, \mathcal{F}\}\} + \{\mathcal{K}, \{\mathcal{F}, \mathcal{G}\}\} = 0, \quad (11)$$

for any three functionals \mathcal{F} , \mathcal{G} , \mathcal{K} . These three properties provide a coordinate-independent abstraction of the essential geometrical properties of Hamilton’s canonical Poisson bracket. The Poisson bracket for the shallow water equations may be written as

$$\{\mathcal{A}, \mathcal{B}\} = \iint d\mathbf{x} \left\{ q \left(\frac{\delta \mathcal{A}}{\delta \tilde{u}} \frac{\delta \mathcal{B}}{\delta \tilde{v}} - \frac{\delta \mathcal{B}}{\delta \tilde{u}} \frac{\delta \mathcal{A}}{\delta \tilde{v}} \right) - \frac{\delta \mathcal{A}}{\delta \tilde{\mathbf{u}}} \cdot \nabla \frac{\delta \mathcal{B}}{\delta h} + \frac{\delta \mathcal{B}}{\delta \tilde{\mathbf{u}}} \cdot \nabla \frac{\delta \mathcal{A}}{\delta h} \right\}, \quad (12)$$

for any pair of functionals \mathcal{A} and \mathcal{B} . This bracket may be rewritten in several different but equivalent forms using integrations by parts [51]. The functional derivatives in (12) are defined with respect to the canonical velocities $\tilde{\mathbf{u}}$ and h , so this bracket reduces to the traditional shallow water Poisson bracket when $\Omega^{(x)} = \Omega^{(y)} = 0$, since $\tilde{\mathbf{u}}$ then equals \mathbf{u} .

The evolution equations (2a)–(2c) may be derived by setting in turn $\mathcal{F} = \tilde{u}(\mathbf{x}_0, t)$, $\mathcal{F} = \tilde{v}(\mathbf{x}_0, t)$, and $\mathcal{F} = h(\mathbf{x}_0, t)$ for a fixed location \mathbf{x}_0 in (10). For example, setting $\mathcal{F} = h_0 = h(\mathbf{x}_0, t)$ in (10) gives

$$\frac{dh_0}{dt} = \{h_0, \mathcal{H}\} = \iint d\mathbf{x} \left\{ q \left(\frac{\delta h_0}{\delta \tilde{u}} \frac{\delta \mathcal{H}}{\delta \tilde{v}} - \frac{\delta \mathcal{H}}{\delta \tilde{u}} \frac{\delta h_0}{\delta \tilde{v}} \right) - \frac{\delta h_0}{\delta \tilde{\mathbf{u}}} \cdot \nabla \frac{\delta \mathcal{H}}{\delta h} + \frac{\delta \mathcal{H}}{\delta \tilde{\mathbf{u}}} \cdot \nabla \frac{\delta h_0}{\delta h} \right\}.$$

For the purpose of taking variational derivatives, $\tilde{\mathbf{u}}$ and h are treated as independent variables so $\delta h_0 / \delta \tilde{\mathbf{u}} = 0$. The particle velocity \mathbf{u} is treated as an explicit function of $\tilde{\mathbf{u}}$ and h , so the variational chain rule gives

$$\frac{\delta \mathcal{H}}{\delta \tilde{\mathbf{u}}} = \frac{\delta \mathcal{H}}{\delta \tilde{\mathbf{u}}}\Big|_{\mathbf{u}} + \left(\frac{\delta \mathcal{H}}{\delta \mathbf{u}} \cdot \frac{\partial \mathbf{u}}{\partial \tilde{u}}, \frac{\delta \mathcal{H}}{\delta \mathbf{u}} \cdot \frac{\partial \mathbf{u}}{\partial \tilde{v}} \right) = \left(\frac{\delta \mathcal{H}}{\delta u}, \frac{\delta \mathcal{H}}{\delta v} \right) = \frac{\delta \mathcal{H}}{\delta \mathbf{u}} = h\mathbf{u}. \quad (13)$$

The notation $|_{\mathbf{u}}$ indicates that \mathbf{u} is held constant while taking the variational derivative with respect to $\tilde{\mathbf{u}}$. Now $\delta h_0 / \delta h$ is nonzero only at $\mathbf{x} = \mathbf{x}_0$, so

$$\frac{dh_0}{dt} = \iint d\mathbf{x} \left\{ \frac{\delta \mathcal{H}}{\delta \tilde{\mathbf{u}}} \cdot \nabla \frac{\delta h(\mathbf{x}_0, t)}{\delta h(\mathbf{x}, t)} \right\} = \iint d\mathbf{x} \left\{ h\mathbf{u} \cdot \nabla \delta(\mathbf{x} - \mathbf{x}_0) \right\}, \quad (14)$$

where $\delta(\mathbf{x} - \mathbf{x}_0)$ is the Dirac delta function in two dimensions. Finally, we integrate by parts and use the divergence theorem with the periodic or no-flux boundary conditions to obtain

$$\frac{d}{dt} h(\mathbf{x}_0, t) = \iint d\mathbf{x} \left\{ -\nabla \cdot (h\mathbf{u}) \delta(\mathbf{x} - \mathbf{x}_0) \right\} = -\nabla \cdot (h\mathbf{u})\Big|_{\mathbf{x}=\mathbf{x}_0}, \quad (15)$$

which is the mass conservation equation (2c).

Symmetries in the variational principle for a Hamiltonian system imply conservation laws via Noether's theorem. The usual momentum and energy conservation laws arising from translation symmetries in space and time. Material conservation of potential vorticity arises from a more subtle relabelling symmetry in the particle-to-label map used to formulate the shallow water equations in Lagrangian coordinates [2, 50, 59, 60]. In the non-canonical Hamiltonian formalism, these conservation laws arise instead from properties of the Poisson bracket. Conservation of energy follows immediately from antisymmetry of the Poisson bracket,

$$\frac{d\mathcal{E}}{dt} = \frac{d\mathcal{H}}{dt} = \{\mathcal{H}, \mathcal{H}\} = 0. \quad (16)$$

Non-canonical Poisson brackets typically support Casimir functionals \mathcal{C} that satisfy

$$\{\mathcal{C}, \mathcal{F}\} = 0 \quad (17)$$

for any functional \mathcal{F} . Two salient Casimir functionals for the shallow water Poisson bracket in (12) are the total mass \mathcal{M} , and the potential enstrophy \mathcal{P} ,

$$\mathcal{M} = \iint d\mathbf{x} \{h\} \quad \text{and} \quad \mathcal{P} = \iint d\mathbf{x} \left\{ \frac{1}{2} h q^2 \right\}. \quad (18)$$

The latter is just one of an infinite family of Casimir functionals of the form

$$\mathcal{C} = \iint d\mathbf{x} \{h c(q)\}, \quad (19)$$

where $c(q)$ is an arbitrary function of the potential vorticity. This family of Casimir functionals thus expresses the material conservation of potential vorticity in an Eulerian setting.

In the following sections we will show that discretizing the non-canonical Hamiltonian formulation of the NTSWE allows us to enforce exact conservation of discrete analogues of the total energy \mathcal{E} , potential enstrophy \mathcal{P} , and total mass \mathcal{M} .

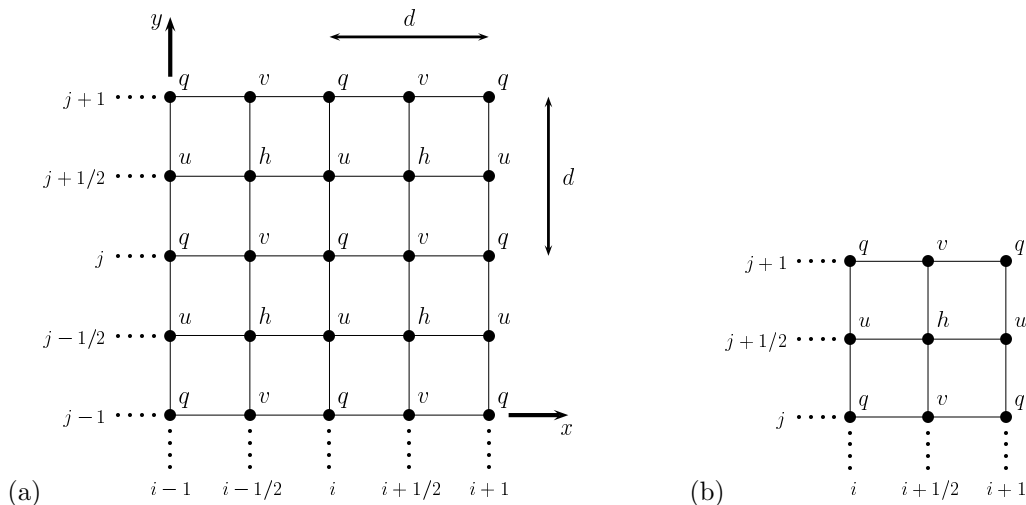


Figure 1: Staggered layout of the variables on the Arakawa C grid. Panel (a) shows the indices of the computational grid and its alignment with the coordinate axes. Panel (b) shows the layout of the variables within a single computational cell.

3. Spatial discretisation

In this section we derive an energy- and potential enstrophy-conserving spatial discretisation for the NTSWE. We begin with a brief review of the Arakawa–Lamb scheme [42] for the single-layer SWE and its Hamiltonian formulation [47], then extend the scheme to the NTSWE, and to multiple layers.

3.1. Hamiltonian formulation of the Arakawa–Lamb scheme

The Arakawa–Lamb [42] scheme for the traditional shallow water equations begins with a staggered placement of the u , v , h and q variables known as the Arakawa C grid, and illustrated in Figure 1. The C grid may be thought of as a mesh of square cells of side length d . The layer thickness h is defined at cell centres, the velocity components are defined at cell faces, and the potential vorticity is defined at cell corners. This layout is optimised for computing the pressure gradient terms in the evolution equations for u and v , and for computing the vorticity as the curl of a two-dimensional velocity field. The velocity components u and v are also naturally placed for computing mass fluxes across cell faces. The schemes presented here generalise straightforwardly to rectangular cells with different side lengths in the x and y directions.

Salmon [47] showed that the Arakawa–Lamb scheme is equivalent to a discrete Hamiltonian system with a discrete Hamiltonian that approximates (9) and a discrete Poisson bracket that approximates (12). Salmon’s discrete Hamiltonian for the Arakawa–Lamb scheme is [47]

$$H = E = \sum_{i,j} \frac{1}{2} h_{i+1/2,j+1/2} \left(\overline{u^2}^x_{i+1/2,j+1/2} + \overline{v^2}^y_{i+1/2,j+1/2} \right) + g h_{i+1/2,j+1/2} (h_b + \frac{1}{2}h)_{i+1/2,j+1/2}. \quad (20)$$

This sum ranges over all cells in the computational grid. We have omitted the factor of d^2 that would make (20) a discrete approximation to a two-dimensional integral $\iint d\mathbf{x}$. This factor cancels with the same omission in our discrete Poisson bracket, which is also a two-dimensional integral $\iint d\mathbf{x}$. The right hand side of (20) is a straightforward discretisation of the total energy (9) on the Arakawa C grid. The kinetic energy terms $\overline{u^2}^x$ and $\overline{v^2}^y$ denote the averages of the contributions from the two u and v points either side of the h point at the centre of each computational cell, as shown in figure 1(b),

$$\overline{u^2}^x_{i+1/2,j+1/2} = \frac{1}{2} \left(u_{i,j+1/2}^2 + u_{i+1,j+1/2}^2 \right), \quad \overline{v^2}^y_{i+1/2,j+1/2} = \frac{1}{2} \left(v_{i+1/2,j}^2 + v_{i+1/2,j+1}^2 \right). \quad (21)$$

The evolution of any function F of the discrete variables $u_{i,j+1/2}$, $v_{i+1/2,j}$, $h_{i+1/2,j+1/2}$ is given by the discrete version of (10)

$$\frac{dF}{dt} = \{F, H\}. \quad (22)$$

We use non-calligraphic symbols for functions of discrete quantities, which approximate the corresponding functionals of continuous field variables written in calligraphic font. Antisymmetry of the discrete Poisson bracket in (22) automatically implies conservation of the discrete energy by the discrete analog of (16)

$$\frac{dE}{dt} = \frac{dH}{dt} = \{H, H\} = 0. \quad (23)$$

The Arakawa–Lamb scheme also conserves the discrete potential enstrophy and discrete total mass defined by

$$P = \sum_{i,j} \bar{h}_{i,j}^{xy} q_{i,j}^2, \quad M = \sum_{i,j} h_{i+1/2,j+1/2}. \quad (24)$$

The discrete potential enstrophy involves the discrete potential vorticity

$$q_{i,j} = \frac{1}{\bar{h}_{i,j}^{xy}} \left(2\Omega_{i,j}^{(z)} + \zeta_{i,j} \right), \quad (25)$$

which contains the natural discrete relative vorticity on the Arakawa C grid,

$$\zeta_{i,j} = \frac{1}{d} (v_{i+1/2,j} - v_{i-1/2,j} - u_{i,j+1/2} + u_{i,j-1/2}), \quad (26)$$

and the natural nearest-neighbour average of h on each q gridpoint,

$$\bar{h}_{i,j}^{xy} = \frac{1}{4} (h_{i+1/2,j+1/2} + h_{i-1/2,j+1/2} + h_{i+1/2,j-1/2} + h_{i-1/2,j-1/2}). \quad (27)$$

As in the continuous theory, conservation of P and M is guaranteed if they are Casimirs of the discrete Poisson bracket, *i.e.*

$$\{F, P\} = \{F, M\} = 0 \quad \text{for any } F(u_{i,j+1/2}, v_{i+1/2,j}, h_{i+1/2,j+1/2}). \quad (28)$$

Here $F(u_{i,j+1/2}, v_{i+1/2,j}, h_{i+1/2,j+1/2})$ denotes an arbitrary function of *all* the u , v and h gridpoints, not just those from one particular grid cell. By the chain rule, this is equivalent to requiring

$$\{u_{i,j+1/2}, P\} = \{v_{i+1/2,j}, P\} = \{h_{i+1/2,j+1/2}, P\} = 0 \quad \text{for all } i, j, \quad (29a)$$

$$\{u_{i,j+1/2}, M\} = \{v_{i+1/2,j}, M\} = \{h_{i+1/2,j+1/2}, M\} = 0 \quad \text{for all } i, j. \quad (29b)$$

Thus the derivation of an energy-, potential enstrophy-, and mass-conserving scheme for the SWE amounts to finding a discretisation of (12) that satisfies (29a) and (29b).

Salmon [47] split the discrete Poisson bracket into a potential vorticity dependent part and a remainder,

$$\{A, B\} = \{A, B\}_Q + \{A, B\}_R, \quad (30)$$

where A and B are algebraic functions of the $u_{i,j+1/2}$, $v_{i+1/2,j}$, and $h_{i+1/2,j+1/2}$ for all i and j . The potential vorticity dependent part is

$$\begin{aligned} \{A, B\}_Q = \sum_{i,j} q_{i,j} \sum_{\mathbf{n}, \mathbf{m}} \left\{ \alpha_{\mathbf{n}, \mathbf{m}} \frac{\partial(A, B)}{\partial(u_{(i,j+1/2)+\mathbf{n}}, v_{(i+1/2,j)+\mathbf{m}})} \right. \\ \left. + \beta_{\mathbf{n}, \mathbf{m}} \frac{\partial(A, B)}{\partial(u_{(i,j+1/2)+\mathbf{n}}, u_{(i,j+1/2)+\mathbf{m}})} + \gamma_{\mathbf{n}, \mathbf{m}} \frac{\partial(A, B)}{\partial(v_{(i+1/2,j)+\mathbf{n}}, v_{(i+1/2,j)+\mathbf{m}})} \right\}, \quad (31) \end{aligned}$$

where

$$\frac{\partial(A, B)}{\partial(u, v)} = \frac{\partial A}{\partial u} \frac{\partial B}{\partial v} - \frac{\partial B}{\partial u} \frac{\partial A}{\partial v} \quad (32)$$

is the Jacobian of A and B with respect to u and v . Again, we omit the factor of d^2 that would make (31) an approximation of the integral in (12). The variational derivatives of the continuous Poisson bracket (12) have become partial derivatives, as in Hamiltonian particle mechanics. The indices $\mathbf{n} = (n_x, n_y)$ and $\mathbf{m} = (m_x, m_y)$ are pairs of integers, and we suppose that the coefficients $\alpha_{\mathbf{m}, \mathbf{n}}$, $\beta_{\mathbf{m}, \mathbf{n}}$, and $\gamma_{\mathbf{m}, \mathbf{n}}$ are only nonzero within a stencil that is $2M + 1$ grid points wide, *i.e.* for $|n_x|, |n_y|, |m_x|, |m_y| \leq M$. The first term proportional to $\alpha_{\mathbf{m}, \mathbf{n}}$ approximates to the term proportional to q in the continuous Poisson bracket (12). The additional terms proportional to $\beta_{\mathbf{n}, \mathbf{m}}$ and $\gamma_{\mathbf{n}, \mathbf{m}}$ introduce the unphysical Coriolis terms in the Arakawa–Lamb scheme that are needed to conserve potential enstrophy [47]. They introduce only an $\mathcal{O}(d^2)$ error, which is consistent with the overall second-order accuracy of the scheme.

The remaining part of the bracket is

$$\begin{aligned} \{A, B\}_R = \frac{1}{d} \sum_{i,j} \left\{ \frac{\partial B}{\partial u_{i,j+1/2}} \left(\frac{\partial A}{\partial h_{i+1/2,j+1/2}} - \frac{\partial A}{\partial h_{i-1/2,j+1/2}} \right) \right. \\ \left. + \frac{\partial B}{\partial v_{i+1/2,j}} \left(\frac{\partial A}{\partial h_{i+1/2,j+1/2}} - \frac{\partial A}{\partial h_{i+1/2,j-1/2}} \right) - (A \longleftrightarrow B) \right\}, \quad (33) \end{aligned}$$

where $(A \longleftrightarrow B)$ indicates that all the preceding terms in (33) should be repeated with A and B exchanged to enforce the anti-symmetry. We have discretised the gradient ∇ in the continuous Poisson bracket (12) using second-order central finite differences.

The coefficients $\alpha_{\mathbf{n}, \mathbf{m}}$, $\beta_{\mathbf{n}, \mathbf{m}}$ and $\gamma_{\mathbf{n}, \mathbf{m}}$ in (31) must now be chosen to satisfy (29a) and (29b), so that P and M are Casimirs. The mass M satisfies condition (29b) for any $\alpha_{\mathbf{n}, \mathbf{m}}$, $\beta_{\mathbf{n}, \mathbf{m}}$ and $\gamma_{\mathbf{n}, \mathbf{m}}$ because $\partial M / \partial u_{i,j+1/2} = \partial M / \partial v_{i+1/2,j} = 0$ and $\partial M / \partial h_{i+1/2,j+1/2} = 1$. There are infinitely many suitable combinations of $\alpha_{\mathbf{n}, \mathbf{m}}$, $\beta_{\mathbf{n}, \mathbf{m}}$, and $\gamma_{\mathbf{n}, \mathbf{m}}$ that conserve potential enstrophy P [47], but for the purpose of illustration we restrict our attention to the coefficients that give the original Arakawa–Lamb scheme [42]. These are listed in the Appendix. Combining (20), (22), and (30) recovers the discrete evolution equations for $u_{i,j+1/2}(t)$, $v_{i+1/2,j}(t)$, and $h_{i+1/2,j+1/2}(t)$ derived by Arakawa & Lamb [42],

$$\frac{d}{dt} h_{i+1/2,j+1/2} = -\frac{1}{d} \left(u_{i+1,j+1/2}^* - u_{i,j+1/2}^* + v_{i+1/2,j+1}^* - v_{i+1/2,j}^* \right), \quad (34a)$$

$$\begin{aligned} \frac{d}{dt} u_{i,j+1/2} = \sum_{k,l} v_{k+1/2,l}^* \sum_{\mathbf{n}, \mathbf{m}} \delta_{(i,j)-(k,l)+\mathbf{m}-\mathbf{n}} \alpha_{\mathbf{n}, \mathbf{m}} q_{(k,l)-\mathbf{m}} \\ + \sum_{k,l} u_{k,l+1/2}^* \sum_{\mathbf{n}, \mathbf{m}} \delta_{(i,j)-(k,l)+\mathbf{m}-\mathbf{n}} (\beta_{\mathbf{n}, \mathbf{m}} - \beta_{\mathbf{m}, \mathbf{n}}) q_{(k,l)-\mathbf{m}} - \frac{1}{d} (\Phi_{i+1/2,j+1/2} - \Phi_{i-1/2,j+1/2}), \quad (34b) \end{aligned}$$

$$\begin{aligned} \frac{d}{dt} v_{i+1/2,j} = -\sum_{k,l} u_{k,l+1/2}^* \sum_{\mathbf{n}, \mathbf{m}} \delta_{(i,j)-(k,l)+\mathbf{n}-\mathbf{m}} \alpha_{\mathbf{n}, \mathbf{m}} q_{(k,l)-\mathbf{n}} \\ + \sum_{k,l} v_{k+1/2,l}^* \sum_{\mathbf{n}, \mathbf{m}} \delta_{(i,j)-(k,l)+\mathbf{m}-\mathbf{n}} (\gamma_{\mathbf{n}, \mathbf{m}} - \gamma_{\mathbf{m}, \mathbf{n}}) q_{(k,l)-\mathbf{m}} - \frac{1}{d} (\Phi_{i+1/2,j+1/2} - \Phi_{i+1/2,j-1/2}), \quad (34c) \end{aligned}$$

where $\delta_{i,j}$ is the Kronecker delta. The discrete Bernoulli potential is

$$\Phi_{i+1/2,j+1/2} = \frac{\partial H}{\partial h_{i+1/2,j+1/2}} = \frac{1}{2} \overline{u^2}^x_{i+1/2,j+1/2} + \frac{1}{2} \overline{v^2}^y_{i+1/2,j+1/2} + g(h_b + h)_{i+1/2,j+1/2}, \quad (35)$$

using the averages $\overline{u^2}^x_{i+1/2,j+1/2}$ and $\overline{v^2}^y_{i+1/2,j+1/2}$ defined in (21). The mass fluxes across cell boundaries

are

$$u_{i,j+1/2}^* = \frac{\partial H}{\partial u_{i,j+1/2}} = \frac{1}{2} \left(h_{i-1/2,j+1/2} + h_{i+1/2,j+1/2} \right) u_{i,j+1/2}, \quad (36a)$$

$$v_{i+1/2,j}^* = \frac{\partial H}{\partial v_{i+1/2,j}} = \frac{1}{2} \left(h_{i+1/2,j-1/2} + h_{i+1/2,j+1/2} \right) v_{i+1/2,j}, \quad (36b)$$

which involve the natural averages of the h values either side of the u or v point.

3.2. Extension to the non-traditional shallow water equations

The Hamiltonian and Poisson bracket for the NTSWE are formulated using the canonical velocity $\tilde{\mathbf{u}}$ and layer thickness h as independent variables. The particle velocity \mathbf{u} is treated as a known function of $\tilde{\mathbf{u}}$ and h via (4). The first step in constructing a discretisation of the NTSWE is therefore to define a discrete canonical velocity. We assign the discrete canonical and particle velocity components to the same grid points, so $u_{i,j+1/2}$ and $v_{i+1/2,j}$ are collocated with $\tilde{u}_{i,j+1/2}$ and $\tilde{v}_{i+1/2,j}$ respectively (see Figure 1). We then define the particle velocity components $u_{i,j+1/2}$ and $v_{i+1/2,j}$ using two arbitrarily-weighted averages over the h points,

$$u_{i,j+1/2} = \tilde{u}_{i,j+1/2} - \sum_{r,s} \mu_{r,s} \left[2\Omega^{(y)} \left(h_b + \frac{1}{2}h \right) \right]_{i+1/2+r,j+1/2+s}, \quad (37a)$$

$$v_{i+1/2,j} = \tilde{v}_{i+1/2,j} + \sum_{r,s} \xi_{r,s} \left[2\Omega^{(x)} \left(h_b + \frac{1}{2}h \right) \right]_{i+1/2+r,j+1/2+s}. \quad (37b)$$

The summations are taken over all integers r and s . The weights $\mu_{r,s}$ and $\xi_{r,s}$ must be chosen so that (37a)–(37b) are consistent with the continuous relations (4) to at least second order in d . We take $\mu_{r,s} = \xi_{r,s} = 0$ for $|r|, |s| > M$, where M defines our stencil size as before. As in our continuous Hamiltonian formulation of the NTSWE, we define the discrete potential and relative vorticities using the canonical velocity components as

$$q_{i,j} = \frac{1}{\bar{h}_{i,j}^{xy}} \left(2\Omega_{i,j}^{(z)} + \tilde{\zeta}_{i,j} \right), \quad \tilde{\zeta}_{i,j} = \frac{1}{d} \left(\tilde{v}_{i+1/2,j} - \tilde{v}_{i-1/2,j} - \tilde{u}_{i,j+1/2} + \tilde{u}_{i,j-1/2} \right). \quad (38)$$

It is implicit in (37a)–(37b) and (38) that the horizontal components $\Omega^{(x)}$ and $\Omega^{(y)}$ of the rotation vector are defined on the h points, while the vertical component $\Omega^{(z)}$ is defined on the q points.

As discussed in §2, the total energy is not changed by the Coriolis force, whether traditional or non-traditional. We therefore use exactly the same discrete Hamiltonian (20) for the non-traditional equations, but now treat $u_{i,j+1/2}$ and $v_{i+1/2,j}$ as explicit functions of $\tilde{u}_{i,j+1/2}, \tilde{v}_{i+1/2,j}, h_{i+1/2,j+1/2}$ via (37a)–(37b). We pose a discretisation of the non-traditional Poisson bracket (12) that is analogous to (30)–(31) for the traditional Poisson bracket,

$$\begin{aligned} \{A, B\}_Q = & \sum_{i,j} q_{i,j} \sum_{\mathbf{n}, \mathbf{m}} \left\{ \alpha_{\mathbf{n}, \mathbf{m}} \frac{\partial(A, B)}{\partial(\tilde{u}_{(i,j+1/2)+\mathbf{n}}, \tilde{v}_{(i+1/2,j)+\mathbf{m}})} \right. \\ & \left. + \beta_{\mathbf{n}, \mathbf{m}} \frac{\partial(A, B)}{\partial(\tilde{u}_{(i,j+1/2)+\mathbf{n}}, \tilde{u}_{(i,j+1/2)+\mathbf{m}})} + \gamma_{\mathbf{n}, \mathbf{m}} \frac{\partial(A, B)}{\partial(\tilde{v}_{(i+1/2,j)+\mathbf{n}}, \tilde{v}_{(i+1/2,j)+\mathbf{m}})} \right\}, \end{aligned} \quad (39a)$$

$$\begin{aligned} \{A, B\}_R = & \frac{1}{d} \sum_{i,j} \left\{ \frac{\partial B}{\partial \tilde{u}_{i,j+1/2}} \left(\frac{\partial A}{\partial h_{i+1/2,j+1/2}} - \frac{\partial A}{\partial h_{i-1/2,j+1/2}} \right) \right. \\ & \left. + \frac{\partial B}{\partial \tilde{v}_{i+1/2,j}} \left(\frac{\partial A}{\partial h_{i+1/2,j+1/2}} - \frac{\partial A}{\partial h_{i+1/2,j-1/2}} \right) - (A \leftrightarrow B) \right\}. \end{aligned} \quad (39b)$$

The only difference is the replacement of u and v by \tilde{u} and \tilde{v} . The discrete dynamics are still given by (22), so it follows from the antisymmetry of the Poisson bracket (39a)–(39b) that (23) still holds, and so the

discrete energy E is conserved. The total potential enstrophy P and mass M are given by (24), but now with the potential vorticity $q_{i,j}$ expressed in terms of \tilde{u} and \tilde{v} through (38). As in the traditional case, P and M are Casimirs of the non-traditional bracket (39a)–(39b) if they satisfy

$$\{\tilde{u}_{i,j+1/2}, P\} = \{\tilde{v}_{i+1/2,j}, P\} = \{h_{i+1/2,j+1/2}, P\} = 0 \quad \text{for all } i, j, \quad (40a)$$

$$\{\tilde{u}_{i,j+1/2}, M\} = \{\tilde{v}_{i+1/2,j}, M\} = \{h_{i+1/2,j+1/2}, M\} = 0 \quad \text{for all } i, j. \quad (40b)$$

The conditions (40a)–(40b) and Poisson bracket (39a)–(39b) are exactly isomorphic to the traditional conditions (29a)–(29b) and Poisson bracket (31) and (33) after replacing u and v by \tilde{u} and \tilde{v} . Any choice of $\alpha_{\mathbf{n},\mathbf{m}}$, $\beta_{\mathbf{n},\mathbf{m}}$, and $\gamma_{\mathbf{n},\mathbf{m}}$ that satisfies (29a)–(29b) also satisfies (40a)–(40b). For the purpose of illustration we use the coefficients corresponding to the original Arakawa–Lamb scheme [42], as given in the Appendix.

It now only remains to find explicit evolution equations for $\tilde{u}_{i,j+1/2}$, $\tilde{v}_{i+1/2,j}$ and $h_{i+1/2,j+1/2}$ from (22) using the discrete Hamiltonian (20) and Poisson bracket (39a)–(39b). For example,

$$\frac{d}{dt}\tilde{u}_{k,l+1/2} = \{\tilde{u}_{k,l+1/2}, H\} = \{\tilde{u}_{k,l+1/2}, H\}_Q + \{\tilde{u}_{k,l+1/2}, H\}_R, \quad (41a)$$

$$\frac{d}{dt}\tilde{v}_{k+1/2,l} = \{\tilde{v}_{k+1/2,l}, H\} = \{\tilde{v}_{k+1/2,l}, H\}_Q + \{\tilde{v}_{k+1/2,l}, H\}_R, \quad (41b)$$

$$\frac{d}{dt}h_{k+1/2,l+1/2} = \{h_{k+1/2,l+1/2}, H\} = \{h_{k+1/2,l+1/2}, H\}_Q + \{h_{k+1/2,l+1/2}, H\}_R, \quad (41c)$$

for integers k and l . The Hamiltonian H depends on $\tilde{\mathbf{u}}$ only through \mathbf{u} , so by the chain rule

$$\frac{\partial H}{\partial \tilde{u}_{k,l+1/2}} = \frac{\partial H}{\partial u_{k,l+1/2}} \frac{\partial u_{k,l+1/2}}{\partial \tilde{u}_{k,l+1/2}} = \frac{\partial H}{\partial u_{k,l+1/2}} = u_{k,l+1/2}^*, \quad (42a)$$

$$\frac{\partial H}{\partial \tilde{v}_{k+1/2,l}} = \frac{\partial H}{\partial v_{k+1/2,l}} \frac{\partial v_{k+1/2,l}}{\partial \tilde{v}_{k+1/2,l}} = \frac{\partial H}{\partial v_{k+1/2,l}} = v_{k+1/2,l}^*. \quad (42b)$$

Thus the contribution of $\{\tilde{u}_{k,l+1/2}, H\}_Q$ to the non-traditional discrete equations is identical to the contribution of $\{u_{k,l+1/2}, H\}_Q$ to the traditional discrete equations. The same is true for $\{\tilde{v}_{k+1/2,l}, H\}_Q$, $\{\tilde{h}_{k+1/2,l+1/2}, H\}_Q$, and $\{\tilde{h}_{k+1/2,l+1/2}, H\}_R$. However, the remaining parts of the discrete evolution equations (41a)–(41c), $\{\tilde{u}_{k,l+1/2}, H\}_R$ and $\{\tilde{v}_{k+1/2,l}, H\}_R$, introduce additional terms via the dependence of u and v on h ,

$$\left. \frac{\partial H}{\partial h_{k+1/2,l+1/2}} \right|_{\tilde{\mathbf{u}}} = \left. \frac{\partial H}{\partial h_{k+1/2,l+1/2}} \right|_{\mathbf{u}} + \sum_{i,j} \left\{ \frac{\partial H}{\partial u_{i,j+1/2}} \frac{\partial u_{i,j+1/2}}{\partial h_{k+1/2,l+1/2}} + \frac{\partial H}{\partial v_{i+1/2,j}} \frac{\partial v_{i+1/2,j}}{\partial h_{k+1/2,l+1/2}} \right\}. \quad (43)$$

Here the subscript $|_{\tilde{\mathbf{u}}}$ indicates that all the u and v values at grid points should be held constant in the derivative. Equation (43) defines the discrete Bernoulli potential $\Phi_{k+1/2,l+1/2} = \partial H / \partial h_{k+1/2,l+1/2}$. Evaluating the derivatives of \mathbf{u} with respect to h in (43) using (37a)–(37b) yields

$$\frac{\partial u_{i,j+1/2}}{\partial h_{k+1/2,l+1/2}} = -\Omega_{i+1/2,j+1/2}^{(y)} \mu_{i-k,j-l}, \quad \frac{\partial v_{i+1/2,j}}{\partial h_{k+1/2,l+1/2}} = \Omega_{i+1/2,j+1/2}^{(x)} \xi_{i-k,j-l}. \quad (44)$$

The discrete Bernoulli potential may therefore be written as

$$\begin{aligned} \Phi_{i+1/2,j+1/2} &= \frac{1}{2} \bar{u}_{i+1/2,j+1/2}^2 + \frac{1}{2} \bar{v}_{i+1/2,j+1/2}^2 + g(h_b + h)_{i+1/2,j+1/2} \\ &\quad - \Omega_{i+1/2,j+1/2}^{(y)} \sum_{r,s} \mu_{-r,-s} u_{i+r,j+1/2+s}^* + \Omega_{i+1/2,j+1/2}^{(x)} \sum_{r,s} \xi_{-r,-s} v_{i+1/2+r,j+s}^*, \end{aligned} \quad (45)$$

which contains discrete non-traditional terms proportional to weighted averages of the mass fluxes u^* and v^* over the nearby \tilde{u} and \tilde{v} points. Comparison with (37a)–(37b) shows that this is symmetric to the weighted

average over h grid points in the definition of the discrete particle velocities $u_{i,j+1/2}, v_{i+1/2,j}$. Thus (45) is guaranteed to be a second-order accurate approximation to the continuous Bernoulli potential (3), provided the discrete particle velocities (37a)–(37b) give at least a second-order accurate approximation to (4). The choice of the weights $\mu_{r,s}$ and $\xi_{r,s}$ does not impact the conservation properties of the numerical scheme.

For simplicity, we use a second-order two-gridpoint average in (37a)–(37b), which corresponds to $\mu_{0,0} = \mu_{-1,0} = \frac{1}{2}$, $\xi_{0,0} = \xi_{0,-1} = \frac{1}{2}$, and $\mu_{r,s} = \xi_{r,s} = 0$ for all other r and s . The discrete particle velocities are then defined as

$$u_{i,j+1/2} = \tilde{u}_{i,j+1/2} - \overline{2\Omega^{(y)} \left(h_b + \frac{1}{2}h \right)}_{i,j+1/2}^x, \quad (46a)$$

$$v_{i+1/2,j} = \tilde{v}_{i+1/2,j} + \overline{2\Omega^{(x)} \left(h_b + \frac{1}{2}h \right)}_{i+1/2,j}^y, \quad (46b)$$

and the discrete Bernoulli potential becomes

$$\begin{aligned} \Phi_{i+1/2,j+1/2} &= \frac{1}{2} \overline{u^2}^x_{i+1/2,j+1/2} + \frac{1}{2} \overline{v^2}^y_{i+1/2,j+1/2} + g(h_b + h)_{i+1/2,j+1/2} \\ &+ \Omega_{i+1/2,j+1/2}^{(x)} \overline{v^*}^y_{i+1/2,j+1/2} - \Omega_{i+1/2,j+1/2}^{(y)} \overline{u^*}^x_{i+1/2,j+1/2}. \end{aligned} \quad (47)$$

Note that $\Omega^{(x)}$ and $\Omega^{(y)}$ need not be located on h -gridpoints, as implied throughout this section. Locating $\Omega^{(x)}$ on v -gridpoints (*i.e.* $\Omega_{i+1/2,j}^{(x)}$) and $\Omega^{(y)}$ on u -gridpoints (*i.e.* $\Omega_{i,j+1/2}^{(y)}$) is natural for calculating the discrete three-dimensional divergence of $\mathbf{\Omega}$ at the q -points where $\Omega^{(z)}$ is located. The three-dimensional divergence of the rotation vector must vanish for potential vorticity to be materially conserved in the continuously stratified fluid equations [58]. The only effect on our scheme from this change would be to move $\Omega^{(y)}$ and $\Omega^{(x)}$ outside of the averaging operators in (46a)–(46b), and to move them within the averaging operators in (47). For example, the rightmost term in (46a) would become $-2\Omega_{i,j+1/2}^{(y)} \overline{\left(h_b + \frac{1}{2}h \right)}_{i,j+1/2}^x$, and the rightmost term in (47) would become $-\overline{\Omega^{(y)} u^*}^x_{i+1/2,j+1/2}$.

3.3. Extension to multiple layers

The multi-layer shallow water equations describe a stack of layers of immiscible fluids whose densities $\rho^{(k)}$ decrease upwards. We use a superscript (k) to indicate the velocity, thickness, and density of the k^{th} layer, with $k = 1$ corresponding to the top layer and $k = K$ to the bottom. We also define the vertical positions of the interfaces between layers as

$$\eta^{(K+1)} = h_b, \quad \eta^{(k)} = h_b + \sum_{l=k}^{l=K} h^{(l)}. \quad (48)$$

The multi-layer analogue of the Hamiltonian (9) is [28]

$$\mathcal{H} = \mathcal{E} = \sum_{k=1}^K \rho^{(k)} \iint d\mathbf{x} \left\{ \frac{1}{2} h^{(k)} \left[\left(u^{(k)} \right)^2 + \left(v^{(k)} \right)^2 \right] + g h^{(k)} \left(\eta^{(k+1)} + \frac{1}{2} h^{(k)} \right) \right\}. \quad (49)$$

The upper surface $\eta^{(k+1)}$ of the layer below thus appears as an effective bottom topography in the contribution to the Hamiltonian from layer k .

The multi-layer Poisson bracket is just a sum of single-layer brackets weighted by inverse density,

$$\{ \mathcal{A}, \mathcal{B} \} = \sum_{k=1}^K \frac{1}{\rho^{(k)}} \iint d\mathbf{x} \left\{ q^{(k)} \left(\frac{\delta \mathcal{A}}{\delta \tilde{u}^{(k)}} \frac{\delta \mathcal{B}}{\delta \tilde{v}^{(k)}} - \frac{\delta \mathcal{B}}{\delta \tilde{u}^{(k)}} \frac{\delta \mathcal{A}}{\delta \tilde{v}^{(k)}} \right) - \frac{\delta \mathcal{A}}{\delta \tilde{\mathbf{u}}^{(k)}} \cdot \nabla \frac{\delta \mathcal{B}}{\delta h^{(k)}} + \frac{\delta \mathcal{B}}{\delta \tilde{\mathbf{u}}^{(k)}} \cdot \nabla \frac{\delta \mathcal{A}}{\delta h^{(k)}} \right\}. \quad (50)$$

The canonical velocity components in each layer are

$$\tilde{u}^{(k)} = u^{(k)} + 2\Omega^{(y)} \left(\eta^{(k+1)} + \frac{1}{2} h^{(k)} \right), \quad \tilde{v}^{(k)} = v^{(k)} - 2\Omega^{(x)} \left(\eta^{(k+1)} + \frac{1}{2} h^{(k)} \right), \quad (51)$$

and the potential vorticity in each layer is

$$q^{(k)} = \frac{1}{h^{(k)}} \left(2\Omega^{(z)} + \frac{\partial \tilde{v}^{(k)}}{\partial x} - \frac{\partial \tilde{u}^{(k)}}{\partial y} \right). \quad (52)$$

The multi-layer NTSWE may be derived from (49) and (50) by substituting $\mathcal{F} = \tilde{u}^{(k)}$, $\mathcal{F} = \tilde{v}^{(k)}$, and $\mathcal{F} = h^{(k)}$ in turn into (10), as outlined in §3.2. The multi-layer shallow water equations conserve the total energy \mathcal{E} over all layers, and the mass $\mathcal{M}^{(k)}$ and potential enstrophy $\mathcal{P}^{(k)}$ in each layer,

$$\mathcal{P}^{(k)} = \rho^{(k)} \iint d\mathbf{x} \left\{ \frac{1}{2} h^{(k)} \left(q^{(k)} \right)^2 \right\}, \quad \mathcal{M}^{(k)} = \rho^{(k)} \iint d\mathbf{x} \left\{ h^{(k)} \right\}. \quad (53)$$

As in the single-layer case, we derive a numerical scheme for the multi-layer NTSWE via a discretisation of the Hamiltonian and Poisson bracket that conserves discrete analogues of the total mass, energy and potential enstrophy. We discretise the Hamiltonian (49) as

$$H = \sum_{k=1}^K \rho^{(k)} \sum_{i,j} \frac{1}{2} h_{i+1/2,j+1/2}^{(k)} \left[\frac{2}{3} \left(\overline{u^2}_{i+1/2,j+1/2}{}^{xyy} + \overline{v^2}_{i+1/2,j+1/2}{}^{xxy} \right)^{(k)} + \frac{1}{3} \left(\overline{u^2}_{i+1/2,j+1/2}{}^x + \overline{v^2}_{i+1/2,j+1/2}{}^y \right)^{(k)} \right] + g h_{i+1/2,j+1/2}^{(k)} (\eta^{(k)} + \frac{1}{2} h^{(k)})_{i+1/2,j+1/2}. \quad (54)$$

The only qualitative change from the single-layer case lies in the averaging of the squared particle velocity components used to approximate the kinetic energy in each layer. These averages must be taken over a larger stencil in the multi-layer case to avoid an internal symmetric computational instability [43]. For example, the superscripts xyy and xxy correspond to the averages

$$\overline{u^2}_{i+1/2,j+1/2}{}^{xyy} = \frac{1}{4} \left(u_{i+1,j+1/2}^2 + u_{i,j+1/2}^2 \right) + \frac{1}{8} \left(u_{i+1,j+3/2}^2 + u_{i,j+3/2}^2 + u_{i+1,j-1/2}^2 + u_{i,j-1/2}^2 \right), \quad (55a)$$

$$\overline{v^2}_{i+1/2,j+1/2}{}^{xxy} = \frac{1}{4} \left(v_{i+1/2,j+1}^2 + v_{i+1/2,j}^2 \right) + \frac{1}{8} \left(v_{i+3/2,j+1}^2 + v_{i+3/2,j}^2 + v_{i-1/2,j+1}^2 + v_{i-1/2,j}^2 \right). \quad (55b)$$

We pose the discrete Poisson bracket as a sum of a potential vorticity dependent part and a remainder in each layer,

$$\{A, B\} = \sum_{k=1}^K \{A, B\}^{(k)} = \sum_{k=1}^K \{A, B\}_Q^{(k)} + \{A, B\}_R^{(k)}, \quad (56a)$$

$$\{A, B\}_Q^{(k)} = \frac{1}{\rho^{(k)}} \sum_{i,j} q_{i,j}^{(k)} \sum_{\mathbf{n}, \mathbf{m}} \left\{ \alpha_{\mathbf{n}, \mathbf{m}}^{(k)} \frac{\partial(A, B)}{\partial \left(\tilde{u}_{(i,j+1/2)+\mathbf{n}}^{(k)}, \tilde{v}_{(i+1/2,j)+\mathbf{m}}^{(k)} \right)} + \beta_{\mathbf{n}, \mathbf{m}}^{(k)} \frac{\partial(A, B)}{\partial \left(\tilde{u}_{(i,j+1/2)+\mathbf{n}}^{(k)}, \tilde{u}_{(i,j+1/2)+\mathbf{m}}^{(k)} \right)} + \gamma_{\mathbf{n}, \mathbf{m}}^{(k)} \frac{\partial(A, B)}{\partial \left(\tilde{v}_{(i+1/2,j)+\mathbf{n}}^{(k)}, \tilde{v}_{(i+1/2,j)+\mathbf{m}}^{(k)} \right)} \right\}, \quad (56b)$$

$$\{A, B\}_R^{(k)} = \frac{1}{\rho^{(k)} d} \sum_{i,j} \left\{ \frac{\partial B}{\partial \tilde{u}_{i,j+1/2}^{(k)}} \left(\frac{\partial A}{\partial h_{i+1/2,j+1/2}^{(k)}} - \frac{\partial A}{\partial h_{i-1/2,j+1/2}^{(k)}} \right) + \frac{\partial B}{\partial \tilde{v}_{i+1/2,j}^{(k)}} \left(\frac{\partial A}{\partial h_{i+1/2,j+1/2}^{(k)}} - \frac{\partial A}{\partial h_{i+1/2,j-1/2}^{(k)}} \right) - (A \longleftrightarrow B) \right\}, \quad (56c)$$

with coefficients $\alpha_{\mathbf{n}, \mathbf{m}}^{(k)}$, $\beta_{\mathbf{n}, \mathbf{m}}^{(k)}$ and $\gamma_{\mathbf{n}, \mathbf{m}}^{(k)}$ to be determined. The discrete potential vorticity in each layer is defined as

$$q_{i,j}^{(k)} = \frac{1}{h_{i,j}^{(k)}} \left(2\Omega^{(z)} + \tilde{\zeta}_{i,j}^{(k)} \right), \quad \text{where} \quad \tilde{\zeta}_{i,j}^{(k)} = \frac{1}{d} \left(\tilde{v}_{i+1/2,j}^{(k)} - \tilde{v}_{i-1/2,j}^{(k)} - \tilde{u}_{i,j+1/2}^{(k)} + \tilde{u}_{i,j-1/2}^{(k)} \right). \quad (57)$$

The discrete potential enstrophy and mass in each layer are

$$P^{(k)} = \rho^{(k)} \sum_{i,j} \left\{ \frac{1}{2} \overline{h^{(k)}}^{xy}_{i,j} \left(q_{i,j}^{(k)} \right)^2 \right\}, \quad M^{(k)} = \rho^{(k)} \sum_{i,j} \left\{ h_{i+1/2,j+1/2}^{(k)} \right\}. \quad (58)$$

As in the single-layer case, the dynamics of the discrete system are given by (22), where H is the multi-layer Hamiltonian (54). Conservation of energy follows trivially from the antisymmetry of the Poisson bracket (56b)–(56c), so (23) holds for the multi-layer Hamiltonian H . To conserve potential enstrophy $P^{(k)}$ within each layer, it is sufficient to ensure that the Poisson bracket satisfies

$$\left\{ \tilde{u}^{(l)}, P^{(k)} \right\} = \left\{ \tilde{v}^{(l)}, P^{(k)} \right\} = \left\{ h^{(l)}, P^{(k)} \right\} = 0, \quad (59)$$

for all $l = 1, \dots, K$. This requirement may be simplified by recognising that $P^{(k)}$ is a function only of $\tilde{u}^{(k)}$, $\tilde{v}^{(k)}$ and $h^{(k)}$, and that only the k^{th} term of the Poisson bracket (56a) contains derivatives with respect to these variables. Thus (59) reduces to

$$\left\{ \tilde{u}^{(k)}, P^{(k)} \right\}^{(k)} = \left\{ \tilde{v}^{(k)}, P^{(k)} \right\}^{(k)} = \left\{ h^{(k)}, P^{(k)} \right\}^{(k)} = 0. \quad (60)$$

Requirement (60) for the discrete potential enstrophy (58) and Poisson bracket (56b)–(56c) is exactly isomorphic to requirement (29a) for the single-layer potential enstrophy (24) and Poisson bracket (31) and (33). Therefore, we may ensure conservation of potential enstrophy using exactly the same coefficients $\alpha_{\mathbf{n},\mathbf{m}}^{(k)} = \alpha_{\mathbf{n},\mathbf{m}}$, $\beta_{\mathbf{n},\mathbf{m}}^{(k)} = \beta_{\mathbf{n},\mathbf{m}}$ and $\gamma_{\mathbf{n},\mathbf{m}}^{(k)} = \gamma_{\mathbf{n},\mathbf{m}}$ in the multi-layer case as in the single-layer case. For the purpose of illustration we use the coefficients corresponding to the original Arakawa–Lamb scheme, as given in the Appendix. Finally, conservation of mass within each layer again follows from $M^{(k)}$ being independent of all velocity variables, and $\partial M^{(k)} / \partial h_{i+1/2,j+1/2}^{(k)} = \delta_{kl}$ being a Kroenecker delta.

Substituting $F = h_{i+1/2,j+1/2}^{(k)}$, $F = \tilde{u}_{i,j+1/2}^{(k)}$, and $F = \tilde{v}_{i+1/2,j}^{(k)}$ in turn into (22) with the discrete Hamiltonian (54) and Poisson bracket (56a) gives the following scheme for the multi-layer NTSWE:

$$\frac{d}{dt} h_{i+1/2,j+1/2}^{(k)} = -\frac{1}{d} \left(u_{i+1,j+1/2}^{(k)\star} - u_{i,j+1/2}^{(k)\star} + v_{i+1/2,j+1}^{(k)\star} - v_{i+1/2,j}^{(k)\star} \right), \quad (61a)$$

$$\begin{aligned} \frac{d}{dt} \tilde{u}_{i,j+1/2}^{(k)} &= \sum_{r,s} v_{r+1/2,s}^{(k)\star} \sum_{\mathbf{n},\mathbf{m}} \delta_{(i,j)-(r,s)+\mathbf{m}-\mathbf{n}} \alpha_{\mathbf{n},\mathbf{m}} q_{(r,s)-\mathbf{m}}^{(k)} \\ &+ \sum_{r,s} u_{r,s+1/2}^{(k)\star} \sum_{\mathbf{n},\mathbf{m}} \delta_{(i,j)-(r,s)+\mathbf{m}-\mathbf{n}} (\beta_{\mathbf{n},\mathbf{m}} - \beta_{\mathbf{m},\mathbf{n}}) q_{(r,s)-\mathbf{m}}^{(k)} - \frac{1}{d} \left(\Phi_{i+1/2,j+1/2}^{(k)} - \Phi_{i-1/2,j+1/2}^{(k)} \right), \end{aligned} \quad (61b)$$

$$\begin{aligned} \frac{d}{dt} \tilde{v}_{i+1/2,j}^{(k)} &= -\sum_{r,s} u_{r,s+1/2}^{(k)\star} \sum_{\mathbf{n},\mathbf{m}} \delta_{(i,j)-(r,s)+\mathbf{n}-\mathbf{m}} \alpha_{\mathbf{n},\mathbf{m}} q_{(r,s)-\mathbf{n}}^{(k)} \\ &+ \sum_{r,s} v_{r+1/2,s}^{(k)\star} \sum_{\mathbf{n},\mathbf{m}} \delta_{(i,j)-(r,s)+\mathbf{m}-\mathbf{n}} (\gamma_{\mathbf{n},\mathbf{m}} - \gamma_{\mathbf{m},\mathbf{n}}) q_{(r,s)-\mathbf{m}}^{(k)} - \frac{1}{d} \left(\Phi_{i+1/2,j+1/2}^{(k)} - \Phi_{i+1/2,j-1/2}^{(k)} \right). \end{aligned} \quad (61c)$$

The larger averaging stencil in the Hamiltonian (54) determines the mass fluxes

$$u_{i,j+1/2}^{(k)\star} = u_{i,j+1/2}^{(k)} \left(\frac{1}{3} \overline{h^{(k)}}^x_{i,j+1/2} + \frac{2}{3} \overline{h^{(k)}}^{xyy}_{i,j+1/2} \right), \quad (62a)$$

$$v_{i+1/2,j}^{(k)\star} = v_{i+1/2,j}^{(k)} \left(\frac{1}{3} \overline{h^{(k)}}^x_{i+1/2,j} + \frac{2}{3} \overline{h^{(k)}}^{xyy}_{i+1/2,j} \right) \quad (62b)$$

in terms of the particle velocity components

$$u_{i,j+1/2}^{(k)} = \tilde{u}_{i,j+1/2}^{(k)} - \overline{2\Omega^{(y)} \left(\eta^{(k+1)} + \frac{1}{2}h^{(k)} \right)}_{i,j+1/2}^x, \quad (63a)$$

$$v_{i+1/2,j}^{(k)} = \tilde{v}_{i+1/2,j}^{(k)} + \overline{2\Omega^{(x)} \left(\eta^{(k+1)} + \frac{1}{2}h^{(k)} \right)}_{i+1/2,j}^y. \quad (63b)$$

The discrete Bernoulli potential for each layer is

$$\begin{aligned} \Phi_{i+1/2,j+1/2}^{(k)} &= \frac{2}{3} \left(\overline{(u^{(k)})^2}^{xyy}_{i+1/2,j+1/2} + \overline{(v^{(k)})^2}^{xxy}_{i+1/2,j+1/2} \right) \\ &+ \frac{1}{3} \left(\overline{(u^{(k)})^2}^x_{i+1/2,j+1/2} + \overline{(v^{(k)})^2}^y_{i+1/2,j+1/2} \right) \\ &+ g \left[\eta_{i+1/2,j+1/2}^{(k)} + \sum_{l=1}^{l=k+1} \frac{\rho^{(l)}}{\rho^{(k)}} h_{i+1/2,j+1/2}^{(l)} \right] \\ &+ \Omega_{i+1/2,j+1/2}^{(x)} \overline{v^{(l)\star y}}_{i+1/2,j+1/2} - \Omega_{i+1/2,j+1/2}^{(y)} \overline{u^{(l)\star x}}_{i+1/2,j+1/2} \\ &+ \sum_{l=1}^{l=k+1} 2 \frac{\rho^{(l)}}{\rho^{(k)}} \left(\Omega_{i+1/2,j+1/2}^{(x)} \overline{v^{(l)\star y}}_{i+1/2,j+1/2} - \Omega_{i+1/2,j+1/2}^{(y)} \overline{u^{(l)\star x}}_{i+1/2,j+1/2} \right). \end{aligned} \quad (64)$$

3.4. Integration in time

For the numerical experiments below, we integrated the discretised NTSWE or multi-layer NTSWE scheme forward in time using the standard 4th order Runge–Kutta scheme with a constant timestep chosen to satisfy the Courant–Friedrichs–Lewy (CFL) stability condition throughout the integration.

4. Numerical experiments

We first nondimensionalise our equations by writing

$$\mathbf{x} = R_d \hat{\mathbf{x}}, \quad \mathbf{u}^{(k)} = c \hat{\mathbf{u}}^{(k)}, \quad h^{(k)} = H \hat{h}^{(k)}, \quad h_b = H \hat{h}_b, \quad \left(\Omega^{(x)}, \Omega^{(y)}, \Omega^{(z)} \right) = \Omega \left(\hat{\Omega}^{(x)}, \hat{\Omega}^{(y)}, \hat{\Omega}^{(z)} \right), \quad (65)$$

where a hat $\hat{\cdot}$ denotes a dimensionless variable. We use the layer thickness scale H , gravitational acceleration g , and planetary rotation rate Ω to construct the gravity wave speed c , Rossby deformation radius R_d , and non-traditional parameter δ [18, 22, 27]

$$c = \sqrt{gH}, \quad R_d = \frac{c}{2\Omega}, \quad \delta = H/R_d = 2\Omega H/c. \quad (66)$$

The last of these is the aspect ratio based on the deformation radius and thickness scale. It is also the ratio between the change $2\Omega H$ in zonal velocity created by displacing a particle at the equator by a vertical distance H while conserving angular momentum and the gravity wave speed c .

The dimensionless components of the rotation vector at latitude ϕ are

$$\hat{\Omega}^{(x)} = 0, \quad \hat{\Omega}^{(y)} = \cos \phi, \quad \hat{\Omega}^{(z)} = \sin \phi, \quad (67)$$

where we have aligned our x -axis with East to make $\hat{\Omega}^{(x)}$ vanish. We take $\phi = \pi/4$, which corresponds to a latitude of 45°N. However, we have based our deformation radius on Ω rather than $\Omega^{(z)} = \Omega \sin \phi$.

Under this nondimensionalisation, the single-layer shallow water equations become

$$\frac{\partial \hat{\mathbf{u}}}{\partial \hat{t}} + \hat{q} \hat{h} \hat{\mathbf{z}} \times \hat{\mathbf{u}} + \hat{\nabla} \hat{\Phi} = 0, \quad \frac{\partial \hat{h}}{\partial \hat{t}} + \hat{\nabla} \cdot (\hat{h} \hat{\mathbf{u}}) = 0, \quad (68)$$

where the dimensionless canonical velocities are

$$\hat{u} = \hat{u} + \delta \hat{\Omega}^{(y)} \left(\hat{h}_b + \frac{1}{2} \hat{h} \right), \quad \hat{v} = \hat{v} - \delta \hat{\Omega}^{(x)} \left(\hat{h}_b + \frac{1}{2} \hat{h} \right). \quad (69)$$

The dimensionless potential vorticity and Bernoulli potential are

$$\hat{q} = \frac{1}{\hat{h}} \left(\hat{\Omega}^{(z)} + \frac{\partial \hat{v}}{\partial \hat{x}} - \frac{\partial \hat{u}}{\partial \hat{y}} \right), \quad \hat{\Phi} = \frac{1}{2} \hat{u}^2 + \frac{1}{2} \hat{v}^2 + \hat{h}_b + \hat{h} + \frac{1}{2} \delta \hat{h} \left(\hat{\Omega}^{(x)} \hat{v} - \hat{\Omega}^{(y)} \hat{u} \right). \quad (70)$$

We will henceforth drop the hat $\hat{\cdot}$ notation for dimensionless variables.

We choose $H = 1000$ m as a characteristic vertical lengthscale for the ocean, and the Earth's rotation rate is $\Omega \approx 7.3 \times 10^{-5} \text{ rad s}^{-1}$. We take $g = 10^{-3} \text{ m s}^{-2}$ to be a reduced gravity for which our shallow water equations give a “ $1\frac{1}{2}$ -layer” or “equivalent barotropic” description of a relatively thin active layer separated from a much thicker quiescent layer by a small density contrast [18, 20, 17]. These parameters yield a gravity wave speed $c = 1 \text{ m s}^{-1}$, a deformation radius $R_d \approx 6.88$ km, and a non-traditional parameter $\delta \approx 0.145$.

4.1. Single-layer geostrophic adjustment

We first focus on the propagation of inertia-gravity waves, which are substantially modified by the non-traditional component of the Coriolis force. Their group velocity and structure depend on their direction of propagation relative to the horizontal component of the rotation vector [12]. We prescribe an initially motionless layer with an upward bulge in the centre of a square doubly-periodic domain with a side length of 10 deformation radii:

$$u|_{t=0} = 0, \quad v|_{t=0} = 0, \quad h|_{t=0} = 1 + \frac{1}{2} \exp \left[- \left(\frac{4x}{5} \right)^2 - \left(\frac{4y}{5} \right)^2 \right]. \quad (71)$$

Figures 2(a–d) illustrate the generation and propagation of inertia-gravity waves from the collapse of the axisymmetric initial peak. Nonlinear interactions subsequently generate shorter and shorter waves that continue to propagate around the domain for as long as we have been able to evolve them (at least until $t = 1000$) because the total energy is conserved. Figures 2(e) and 2(f) shows the convergence of the numerical solution as we increase the number of gridpoints N along both the x - and y -axes. We quantify the convergence using the discrete ℓ^2 norms of the differences in the potential vorticity (ϵ_q) and layer thickness (ϵ_h) relative to a reference solution computed using a Fourier pseudospectral method with 2048×2048 collocation points, and the Hou–Li spectral filter to provide dissipation at the finest resolved scales [61]. We use the average $\bar{h}_{i,j}^{xy}$ defined in (27) to construct a layer thickness field on the same (i, j) grid points as the potential vorticity (see figure 1). Figures 2(e) shows the expected second-order convergence of the potential vorticity field at the four times $t \in \{5, 10, 15, 20\}$. However, the convergence rate for the layer thickness field deteriorates at later times due to the presence of small-amplitude shock waves [62]. These are created by the nonlinear steepening of the original inertia-gravity waves, and form increasingly more complicated patterns as shocks collide with their periodic images.

The asymmetry along the x -axis in figures 2(c) and 2(d) is due to the East/West asymmetry of the gravity wave dispersion relation created by non-traditional effects [12]. The horizontal component of the rotation vector $\mathbf{\Omega}$ creates a preferred horizontal direction. To explore the consequences of this asymmetry we continued the integration of both the SWE and the NTSWE up to $t = 200$ on a 1024×1024 grid. To distinguish the geostrophically adjusted state from the fluctuations associated with the inertia-gravity waves, which are trapped by the periodic boundary conditions, we plot the average $\langle \dots \rangle$ of each quantity over the time interval from $t = 100$ to $t = 200$. Figure 3 compares the mean layer thickness $\langle h \rangle$ and the layer thickness variance $\langle h'^2 \rangle = \langle h^2 \rangle - \langle h \rangle^2$ between the traditional and non-traditional SWE. Figures 3(a) and 3(b) show that the geostrophically adjusted mean states are almost indistinguishable. However, their variances show significant differences. Figure 3(c) shows that the fluctuations in the traditional shallow water equations are focused at the site of the initial surface displacement and its antipode, and show near-perfect 4-fold rotational symmetry. The slight rotational asymmetry visible may be attributed to the imperfect

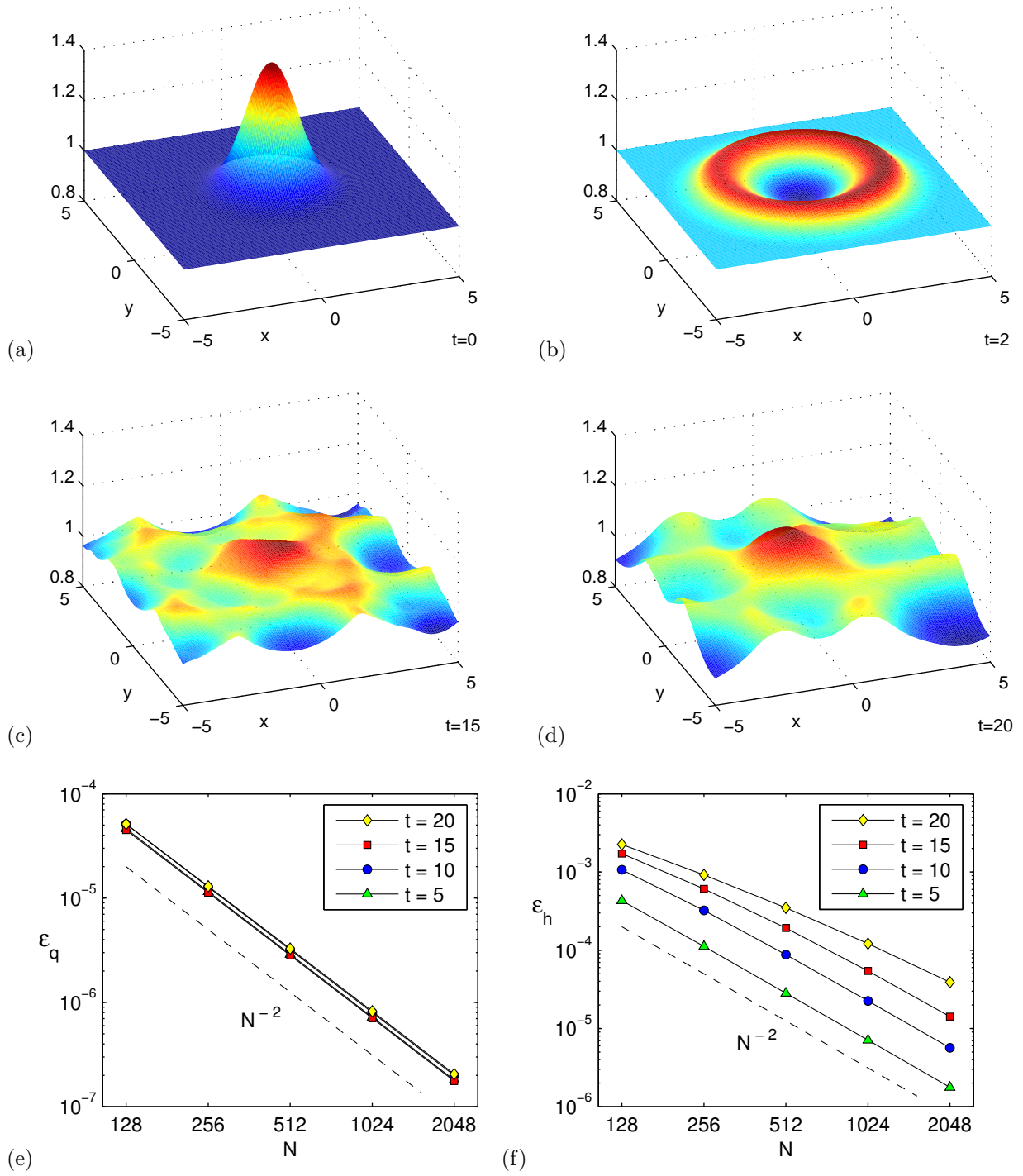


Figure 2: Panels (a–d) show snapshots of the layer thickness h from the single-layer geostrophic adjustment test case described in §4.1 on a 128×128 grid. Convergence in the ℓ^2 norm of (e) the potential vorticity q and (f) the layer thickness h under refinement of the $N \times N$ grid.

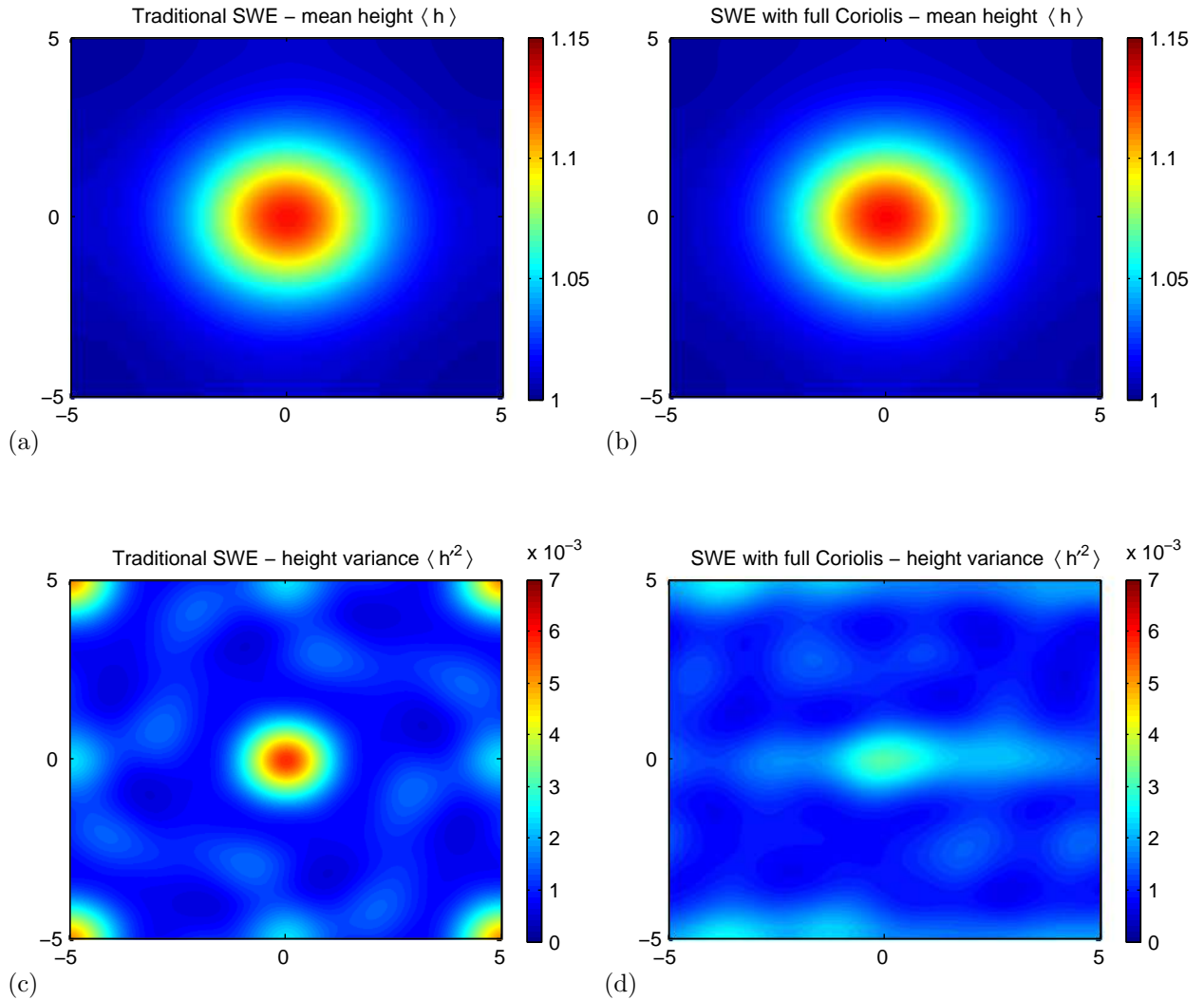


Figure 3: Time-averaged diagnostics from our single-layer geostrophic adjustment test case between $t = 100$ and $t = 200$, computed on a 1024×1024 grid. Panels (a) and (b) compare the time-averaged layer thickness $\langle h \rangle$ in the SWE and NTSWE solutions respectively. Panels (c) and (d) compare the layer thickness variance $\langle h'^2 \rangle$.

cyclone/anticyclone symmetry in the traditional shallow water equations [63]; a simulation in which $\Omega^{(z)}$ has the opposite sign produces the opposite asymmetry. Figure 3(d) shows a much greater loss of 4-fold rotational symmetry due to the non-traditional component of the Coriolis force that spreads the fluctuations into zonal bands.

4.2. Single-layer shear instability

The inertia-gravity waves produced in our first test involve a horizontally divergent flow with relatively large vertical velocities. Our second test instead emphasises the vorticity dynamics of our model. We consider the roll-up of an unstable shear layer that is initially in geostrophic balance, referred to in a geophysical context as a barotropic instability [1]. A velocity field \mathbf{u}_g is in geostrophic balance with the layer thickness

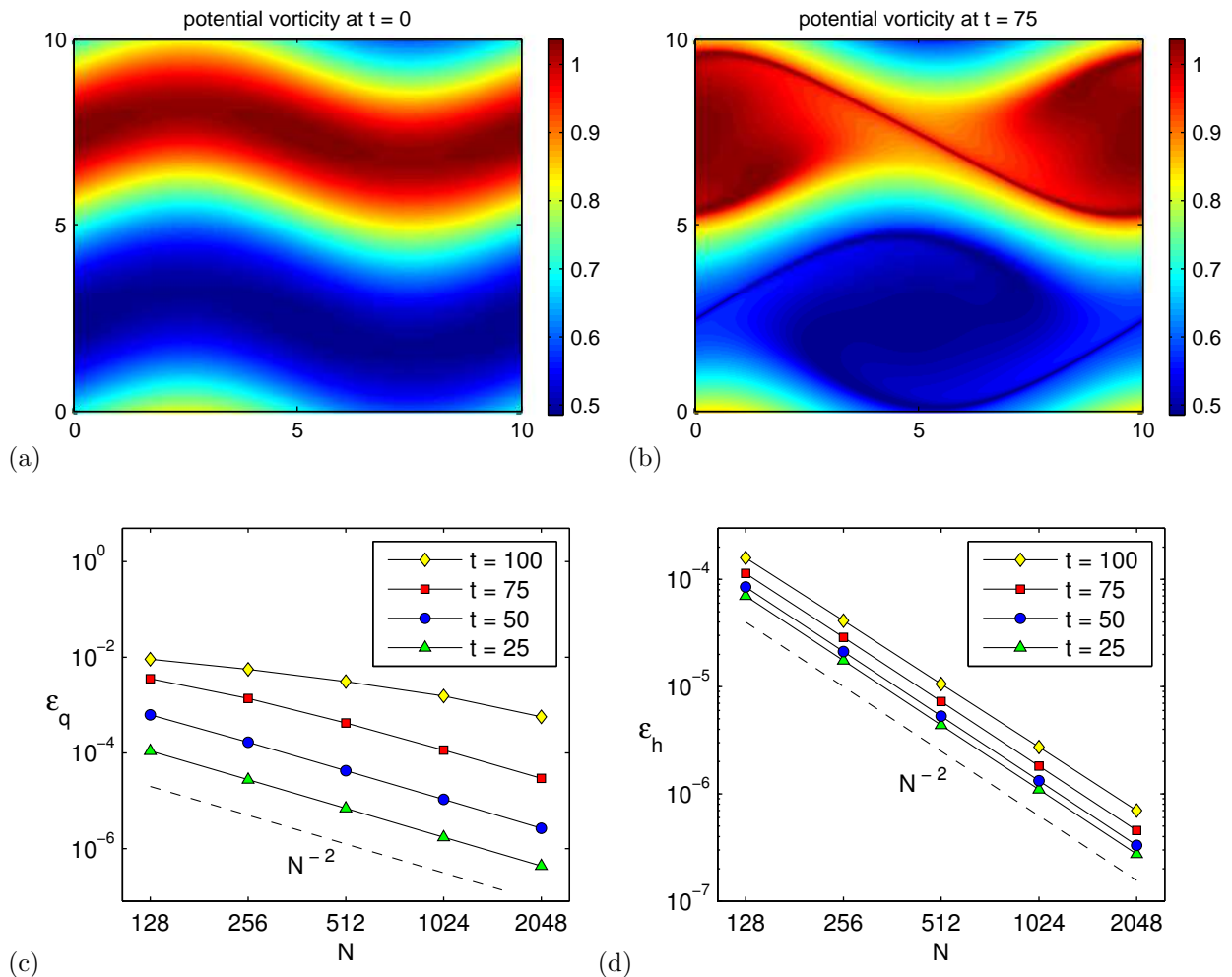


Figure 4: Snapshots of the potential vorticity q from the single-layer shear instability test case described in §4.2 computed on a 1024×1024 grid at (a) $t = 0$ and (b) $t = 75$. Convergence of the ℓ^2 norm of (c) the potential vorticity q and (d) the layer thickness h under refinement of the $N \times N$ spatial grid.

field if the traditional component of the Coriolis force balances the pressure gradient,

$$\Omega^{(z)} \mathbf{z} \times \mathbf{u}_g = \nabla h. \quad (72)$$

This traditional geostrophic relation holds when non-traditional effects are weak ($\delta \ll 1$), the dimensionless velocity is small ($|\mathbf{u}| \ll 1$), and deviations of the layer thickness are small ($|\nabla h| \ll 1$). The latter two conditions are equivalent to smallness of the Rossby and Froude numbers respectively. The geostrophic velocity given by (72) has no horizontal divergence. The vertical velocity component must thus be independent of depth, and hence vanishes when the flow is over a horizontal lower boundary.

We prescribe an initial layer thickness that varies sinusoidally with amplitude $\Delta h = 0.2$ in the y -direction,

and compute the corresponding velocity components from (72),

$$h|_{t=0} = 1 + \Delta h \sin \left\{ \frac{2\pi}{L} \left[y - \Delta y \sin \left(\frac{2\pi x}{L} \right) \right] \right\}, \quad (73a)$$

$$u|_{t=0} = -\frac{2\pi\Delta h}{\Omega^{(z)}L} \cos \left\{ \frac{2\pi}{L} \left[y - \Delta y \sin \left(\frac{2\pi x}{L} \right) \right] \right\}, \quad (73b)$$

$$v|_{t=0} = -\frac{4\pi^2\Delta h\Delta y}{\Omega^{(z)}L^2} \cos \left\{ \frac{2\pi}{L} \left[y - \Delta y \sin \left(\frac{2\pi x}{L} \right) \right] \right\} \cos \left(\frac{2\pi x}{L} \right). \quad (73c)$$

These initial conditions describe an alternating patterns of geostrophic jets in the x -direction whose paths are perturbed by a sinusoidal meander of amplitude $\Delta y = 0.5$ in the y -direction. The model parameters are otherwise the same as in our first test case in §4.1. As before, we take the dimensionless domain length to be $L = 10$, and the reduced gravity to be $g = 10^{-3}\text{m s}^{-2}$, so the non-traditional parameter is $\delta \approx 0.145$

Figure 4(a–b) illustrates the roll-up of the potential vorticity from its initial state until the shear develops filaments on the order of the grid scale. Beyond this point the solution begins to develop spurious grid-scale potential vorticity anomalies, but remains numerically stable (in the sense that it does not blow up) due to the exact conservation of discrete energy and potential enstrophy. Non-traditional effects remain small, because the flow remains close to traditional geostrophic balance, with only a small vertical velocity component. The difference between the SWE and NTSWE solutions is typically on the order of 0.5%. The largest difference over in the domain at $t = 75$ is around 5%, which arises because the non-traditional component of the Coriolis force shifts the PV filaments in Figure 4(b) downward by 0.05–0.1 deformation radii.

Figure 4(c–d) shows the convergence of these solutions to a spectral reference solution under grid refinement. The layer thickness field shows second-order convergence for all times, while the convergence of the potential vorticity field deteriorates at later times due to the formation of extensive grid-scale noise. This is consistent with the potential vorticity q being related to the Laplacian of the layer thickness h for flows in geostrophic balance (72), so h remains smooth even when q develops grid-scale noise.

4.3. Two-layer shear instability

Finally, we test the extension of our scheme to more than one layer described in §3.3 using a two-layer analogue of the problem in §4.2. We take the upper layer to be initially stationary with a flat upper surface,

$$u^{(1)}|_{t=0} = 0, \quad v^{(1)}|_{t=0} = 0, \quad h^{(1)}|_{t=0} = 2 - h^{(2)}. \quad (74)$$

In the lower layer we prescribe an initial jet configuration similar to the one we used in §4.2,

$$u^{(2)}|_{t=0} = -\left(1 - \frac{\rho^{(1)}}{\rho^{(2)}}\right) \frac{2\pi\Delta h}{\Omega^{(z)}L} \cos \left\{ \frac{2\pi}{L} \left[y - \Delta y \sin \left(\frac{2\pi x}{L} \right) \right] \right\}, \quad (75a)$$

$$v^{(2)}|_{t=0} = -\left(1 - \frac{\rho^{(1)}}{\rho^{(2)}}\right) \frac{4\pi^2\Delta h\Delta y}{\Omega^{(z)}L^2} \cos \left\{ \frac{2\pi}{L} \left[y - \Delta y \sin \left(\frac{2\pi x}{L} \right) \right] \right\} \cos \left(\frac{2\pi x}{L} \right), \quad (75b)$$

$$h^{(2)}|_{t=0} = 1 + \Delta h \sin \left\{ \frac{2\pi}{L} \left[y - \Delta y \sin \left(\frac{2\pi x}{L} \right) \right] \right\}. \quad (75c)$$

The initial lower layer velocity and thickness are again in traditional geostrophic balance, since

$$\Omega^{(z)}\mathbf{z} \times \mathbf{u}^{(2)} = \left(1 - \frac{\rho^{(1)}}{\rho^{(2)}}\right) \nabla h^{(2)}. \quad (76)$$

This two-layer configuration includes both horizontal and vertical shear, and so may be unstable to both barotropic and baroclinic instabilities. The latter results from the available potential energy associated with vertical shear in geostrophic flow [1]. As in the previous examples, we use a domain of dimensionless width

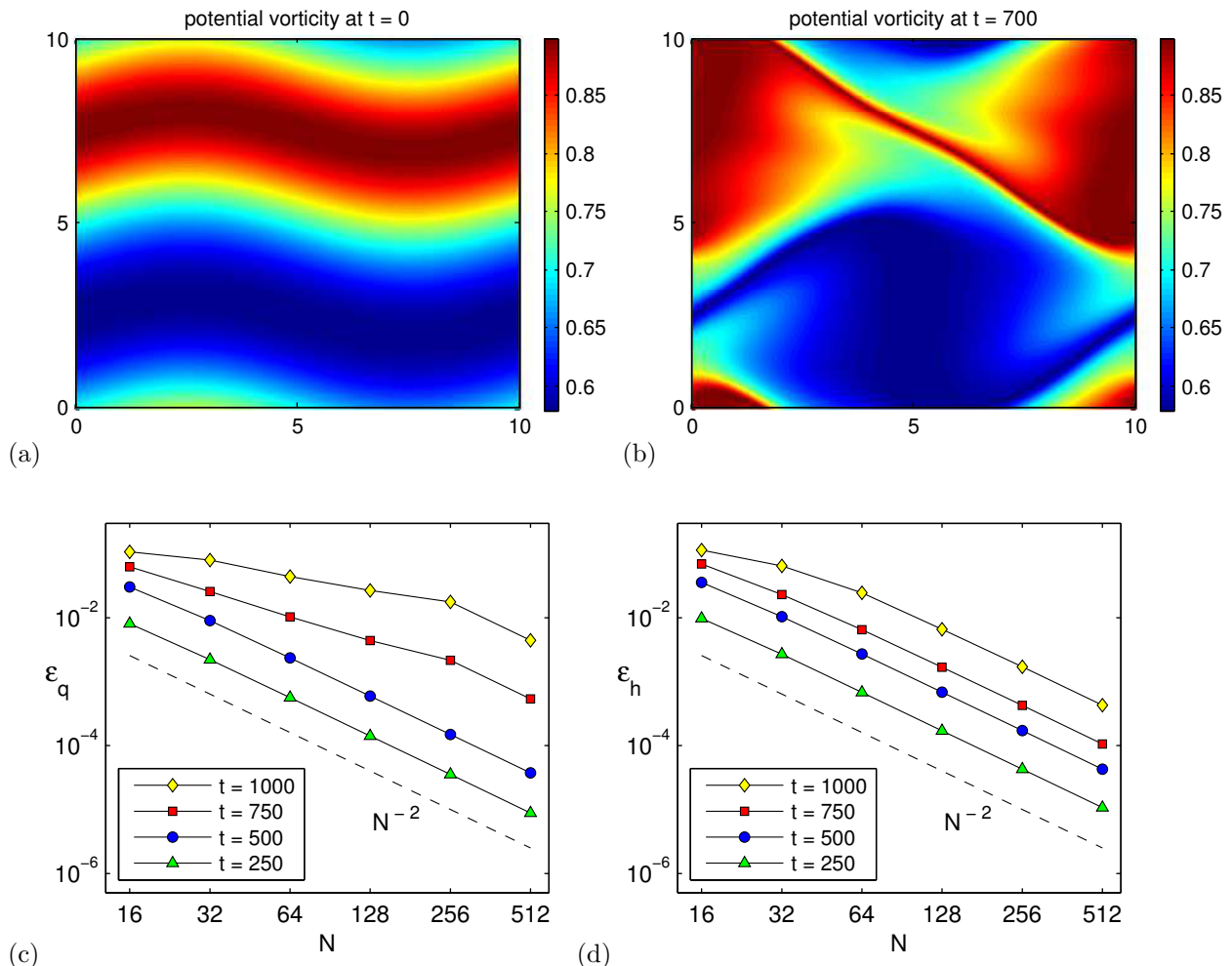


Figure 5: (a,b) Snapshots of the lower-layer potential vorticity $q^{(2)}$ from the two-layer shear instability test case describe in §4.3, with a grid size of $N = 512$. (c,d) Convergence of the L^2 norm of the lower-layer potential vorticity $q^{(2)}$ and layer thickness $h^{(2)}$ with increasing numbers of grid points N .

$L = 10$. We now use a larger reduced gravity $g = 10^{-2} \text{ms}^{-2}$, and a density difference $\rho^{(1)}/\rho^{(2)} = 0.9$, so the effective reduced gravity at the interface between the layers is the same as in §4.2.

Figures 5(a–b) show the lower-layer potential vorticity at $t = 0$ and $t = 700$. These times correspond to the snapshots plotted in Figure 4(a–b) because the dimensionless velocities in (75a)–(75b) are an order of magnitude smaller than in (73b)–(73c). As for the single layer, the flow forms two rolls of potential vorticity with grid-scale filaments around their margins. Figure 5(b) also displays intrusions into the core regions of near-homogeneous potential vorticity, indicating the onset of a secondary baroclinic instability. These features are not substantially modified by the non-traditional Coriolis force. The difference between the traditional and non-traditional solutions is almost identical to the single-layer shear roll-up in §4.2.

Figures 5(c–d) show the convergence of the errors ϵ_q in $q^{(2)}$ and ϵ_h in $h^{(2)}$ under grid refinement. For this test, the reference solution was obtained using Richardson extrapolation from the solutions with $N = 512$ and $N = 1024$. As before, we see second order convergence of the layer thickness field h at all times, but the convergence of the potential vorticity q deteriorates at later times due to the formation of fine scale

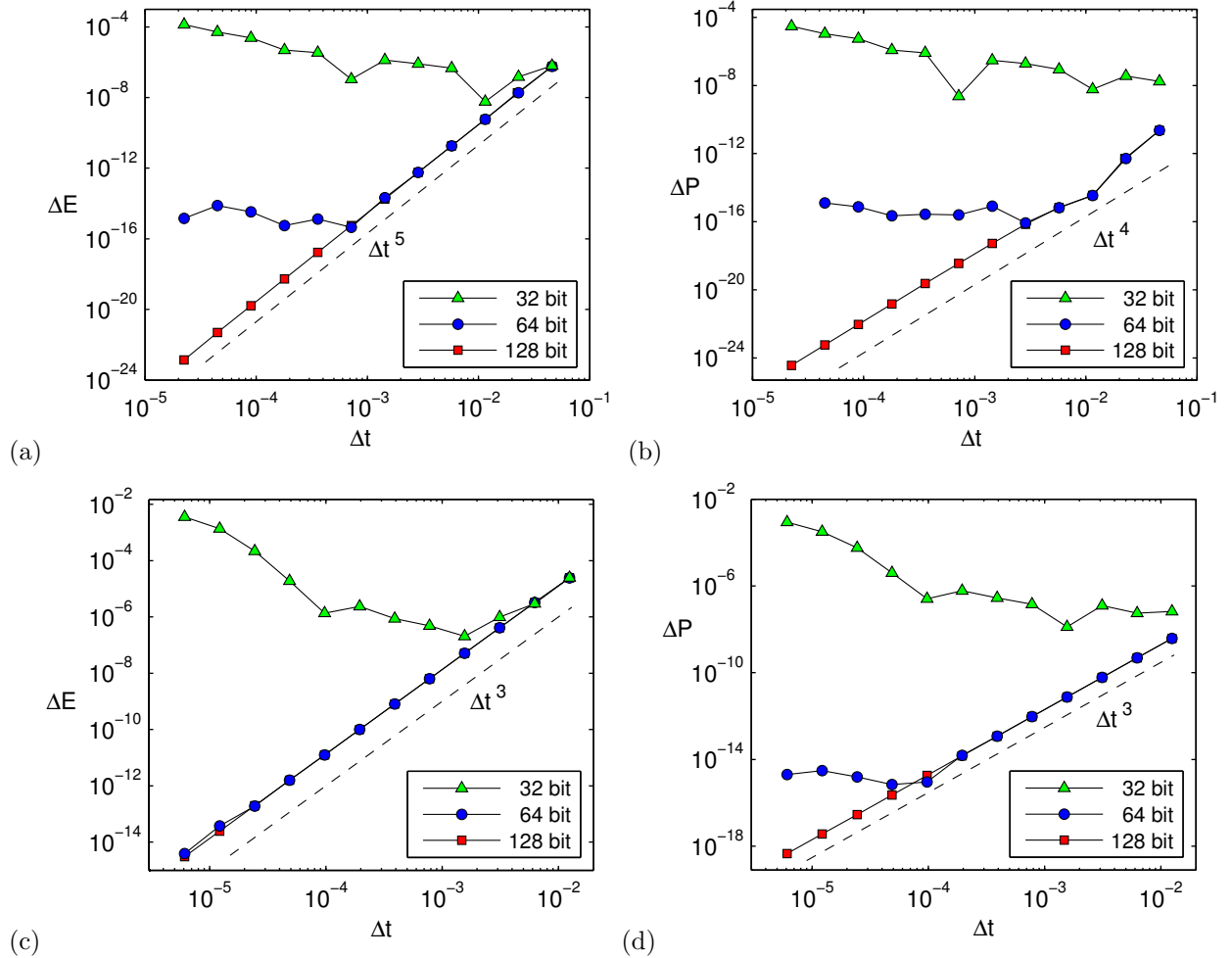


Figure 6: Change in the dimensionless (a,c) energy E and (b,d) potential enstrophy P between $t = 0$ and $t = 1000$ for integrations of the single-layer geostrophic adjustment test case described in §4.1 on a 50×50 grid using three different floating point precisions and the (a,b) 4th order Runge–Kutta and (c,d) 3rd order Adams–Bashforth schemes. In panel (b) the leftmost point (smallest time step) from the 64-bit precision experiments is missing because ΔP is exactly zero under Kahan summation, and so does not appear on a log-log plot.

structures in q .

5. Temporal truncation error

The convergence studies described in §4 demonstrate that the numerical scheme derived in §3 achieves the expected second-order accuracy under spatial grid refinement. However, the exact conservation of the discrete total energy E and potential enstrophy P only holds in the semi-discrete formulation in which the values of u , v , h at grid points evolve according to an ODE system in continuous time. In this section we show that the changes E and P due to the finite accuracy of the time integration may be reduced to machine round-off level by using a sufficiently short time step at fixed spatial resolution. We re-use the IGW propagation problem from §4.1 for which the non-traditional component of the Coriolis force is most prominent. We employ a coarse 50×50 grid for computational efficiency, and to emphasise any changes in E and P due to spatial truncation error.

Figure 6 shows the changes in the instantaneous dimensionless total energy E and potential enstrophy P between $t = 0$ and $t = 1000$ as a function of the dimensionless time step Δt for integrations using either the 4th order Runge–Kutta or the 3rd order Adams–Bashforth schemes [53]. We used the Runge–Kutta scheme to generate the two initial timesteps required by the Adams–Bashforth scheme. We also show results computed using IEEE 32, 64, and 128 bit floating point arithmetic, with precisions of roughly 7, 16, and 34 decimal digits respectively.

The natural calculation of E and P as sums over all grid points involves adding the contribution from one grid point to the accumulated partial sum from previous grid points in the sum. This is susceptible to loss of precision due to the differing magnitudes of the single contribution and the partial sum. The changes in E and P over time are also expected to be small, so the calculation of $\Delta E = E(t = 1000) - E(t = 0)$ and $\Delta P = P(t = 1000) - P(t = 0)$ involves the subtraction of two nearly equal quantities, which is again susceptible to loss of precision.

We found that a straightforward calculation of E and P at the two different times, followed by their subtraction, is subject to an accumulated round-off error several orders of magnitude larger than the error achievable from the same discrete u , v and h fields at grid points using a more accurate summation. In other words, the largest contribution to ΔE and ΔP is the error in their calculation, rather than any inaccuracy in the underlying u , v and h fields.

We therefore computed E and P using the Kahan summation algorithm [64, 65], which compensates for the residual lost when adding a smaller quantity to a larger quantity. For example, when adding two numbers a and b , the Kahan summation algorithm computes s and r such that $a + b = s + r$ holds exactly in binary floating point arithmetic, s is the closest representable floating point approximation to the exact sum $a + b$, and r is the residual. When extended to n terms, Kahan summation has an error bound that is independent of n when n is less than the reciprocal of the machine epsilon. By contrast, the error bound for a straightforward recursive summation grows proportionally to n . We performed the Kahan summation in 64 bit arithmetic for the 32 bit simulations, and otherwise used the same precision as the simulation.

Figures 6(a) and (b) show fifth-order convergence of ΔE , and fourth-order convergence of ΔP , using the 4th order Runge–Kutta scheme. The higher than expected convergence for ΔE with the Runge–Kutta scheme may be because the leading-order truncation error for wavelike phenomena is dispersive, and E involves only sums of the u , v , and h fields at grid points. By contrast, P involves differences between u and v fields at adjacent grid points, and so may be expected to be sensitive to phase differences due to dispersive errors. McRae & Cotter [49] found the same combination of fifth-order convergence for ΔE and fourth-order convergence of ΔP with their finite element spatial discretisation and the same 4th order Runge–Kutta scheme. Figures 6(c–d) show the expected third-order convergence for both ΔE and ΔP with the 3rd order Adams–Bashforth scheme, whose leading order truncation error is dissipative.

In all cases, the achievable accuracy for small Δt is limited by finite floating point precision. Different minima are achievable for ΔE and ΔP due to the different sequences of floating point operations required to compute the two quantities. When using 32 bit arithmetic there is little benefit in reducing Δt below the CFL stability threshold, since ΔE and ΔP are dominated by round-off error, not temporal truncation error. At more realistic spatial resolutions, such as 1024×1024 , for which Δt must be substantially reduced to satisfy the CFL stability condition, the largest stable Δt will typically produce ΔE and ΔP comparable to round-off error in 64 bit arithmetic.

6. Conclusion

We have extended the energy and potential enstrophy conserving properties of the Arakawa–Lamb [42] scheme to the multi-layer non-traditional shallow water equations (NTSWE) that include a depth-averaged treatment of the complete Coriolis force [27, 28]. These conservation properties help to prevent a spurious forward energy cascade to the finest resolved scales, and suppress nonlinear numerical instabilities. They seem essential for correctly simulating the inverse energy cascade in two-dimensional turbulence, and improve material conservation of potential vorticity in Eulerian grid-based schemes [37].

Salmon [47] showed that the Arakawa–Lamb scheme is equivalent to the Hamiltonian system formed by discretising the Hamiltonian and Poisson bracket for a non-canonical Hamiltonian formulation of the

shallow water equations (SWE). Discrete energy conservation then follows immediately from antisymmetry of the discrete Poisson bracket via (23). By contrast, the SWE conserve potential enstrophy because it is a Casimir functional of the non-canonical Poisson bracket, so its bracket with any other functional vanishes. Salmon [47] constructed a discrete Poisson bracket for which a discrete analog of the potential enstrophy is also a Casimir.

We were able to reuse much of Salmon’s approach because the shallow water equations with no rotation, traditional rotation, and non-traditional rotation may all be written in non-canonical Hamiltonian form using the same Poisson bracket by distinguishing between the particle velocity \mathbf{u} and the canonical velocity $\tilde{\mathbf{u}}$. The particle velocity appears in the mass conservation equation and the Bernoulli potential. The kinetic energy in the Hamiltonian is calculated from the square of the particle velocity, and is unaffected by rotation. The canonical velocity may be derived from the layer average of the three-dimensional velocity vector $\mathbf{u} + \boldsymbol{\Omega} \times \mathbf{x}$ relative to an inertial frame by applying a gauge transformation to remove the vertical component [27, 28]. Its time derivative appears in the vector invariant form of the momentum equation, and its curl defines the materially-conserved potential vorticity. However, the distinction between these two velocities is commonly elided in the traditional shallow water equations, because they differ only by a function of position so their time derivatives are equal.

By contrast, the canonical velocity for the NTSWE contains additional terms proportional to the evolving layer depth $h(\mathbf{x}, t)$ and the horizontal components $\Omega^{(x)}$ and $\Omega^{(y)}$ of the rotation vector. The Poisson bracket is formulated for h and $\tilde{\mathbf{u}}$ as independent variables, but the Hamiltonian contains \mathbf{u} , which we treat as a known function of h and $\tilde{\mathbf{u}}$. We place the particle and canonical velocity components at the same locations in the staggered Arakawa C grid that underlies the Arakawa–Lamb scheme. Since the layer depth h is not collocated with any of these variables, we needed to construct averages of h at the u and v points (see figure 1). We used simple averages of the two u or v points adjacent to each h point.

Turning to the multi-layer system, its Poisson bracket may be written as a sum of uncoupled Poisson brackets, each involving only the canonical velocity $\tilde{\mathbf{u}}^{(k)}$ and depth $h^{(k)}$ of the k^{th} layer. Coupling between layers occurs only through the Hamiltonian, in which the upper surface of each layer appears as an effective bottom topography for the layer immediately above. This decomposition enabled us to construct a discretisation that conserves a discrete total energy for the whole system, and the discrete masses and potential enstrophies within individual layers. However, a widening of the averaging stencil used to compute the discrete kinetic energy within each layer is required to avoid spurious internal computational symmetric instabilities [43]. This implies a wider averaging stencil for the discrete mass fluxes and Bernoulli potentials in the resulting evolution equations.

In §4 we verified through numerical experiments that our scheme consistently exhibits at least second-order convergence of the potential vorticity and layer thickness fields under grid refinement for both one and two layers. The influence of the non-traditional Coriolis force is most obvious in the geostrophic adjustment test case described in §4.1. There is little difference in the geostrophically adjusted states approached by the SWE and NTSWE, but the fluctuations associated with propagating inertia-gravity waves are qualitatively different due to the horizontal anisotropy in the inertia-gravity wave dispersion relation created by the horizontal component of the rotation vector [12]. In our shear instability test cases (§4.2 and §4.3) the flows are largely geostrophically balanced, so vertical motions and the non-traditional Coriolis force are minimised.

The Arakawa–Lamb scheme and our non-traditional extension are both semi-discrete schemes. They express the evolution of grid point values of velocity and layer thickness in continuous time, and the conservation properties for mass, energy, and potential enstrophy also hold in continuous time. In §5 we demonstrated that total energy and potential enstrophy can indeed be conserved down to machine round-off error by using standard time integration schemes with a sufficiently short timestep. We observed the expected 3rd order convergence of the conserved quantities for the 3rd order Adams–Bashforth scheme. For the 4th order Runge–Kutta scheme we found 5th order convergence of the energy and 4th order convergence of the potential enstrophy, in agreement with similar experiments recently performed with a finite element spatial discretisation [49].

The schemes and test cases discussed here are all valid in the absence of lateral boundaries. The Arakawa–Lamb scheme for the traditional single-layer SWE has been modified to include arbitrary lateral boundaries by rewriting the discrete energy and vorticity equations in flux form, and imposing physical boundary

conditions on the fluxes [66, 67]. This approach should extend to our scheme for the single-layer NTSWE, but becomes more complicated for multiple layers due to the larger grid stencil used for the mass fluxes. Incorporating boundary conditions into a multi-layer scheme may be more easily accomplished in a vorticity, divergence, and depth formulation in which the boundary conditions only enter the elliptic equations needed to solve for the velocity potential and streamfunction used to represent the velocity within each layer [56, 68].

Though in principle our numerical scheme permits arbitrary lateral variation of the components of the rotation vector $\mathbf{\Omega}$ [58], all of our numerical test cases in §4 use constant values for these components. We have separately tested the scheme with spatially-varying $\Omega^{(z)}$ and constant $\Omega^{(x)}$ and $\Omega^{(y)}$, similar to the Grimshaw [69] β -plane and found that energy and potential energy are conserved to similar precision as in §5. However, in this article we have not explored the performance of our scheme with spatially-varying $\mathbf{\Omega}$.

Our energy- and potential enstrophy-conserving scheme for the NTSWE has broad utility for modelling large-scale geophysical flows using layer-based or isopycnal coordinate numerical models with a complete treatment of the Coriolis force. By construction, the NTSWE prevent exchanges of mass and tracers across density surfaces, unless these are explicitly imposed. It would be straightforward to retrofit isopycnal models to incorporate the full Coriolis force using the scheme described in this paper. The authors foresee this scheme being of practical use for the exploration of oceanic phenomena likely to be influenced by the non-traditional component of the Coriolis force, such as internal wave generation over topographic features [12] or abyssal currents flowing close to the equator [18, 19, 20].

Acknowledgements

Some of the computations employed the Advanced Research Computing (ARC) facility at the University of Oxford [70]. The authors thank the three anonymous reviewers for their constructive comments on the manuscript.

Appendix A. Coefficients of the Discrete Poisson Bracket

The discrete Poisson bracket (31) contains three families of coefficients $\alpha_{\mathbf{n},\mathbf{m}}$, $\beta_{\mathbf{n},\mathbf{m}}$ and $\gamma_{\mathbf{n},\mathbf{m}}$ that must be chosen to ensure conservation of the discrete potential enstrophy. The nonvanishing coefficients for the Arakawa–Lamb scheme are [47]

$$\alpha_{(0,0)(0,1)} = \alpha_{(0,0)(-1,1)} = \alpha_{(0,-1)(0,-1)} = \alpha_{(0,-1)(-1,-1)} = 1/12, \quad (\text{A.1a})$$

$$\alpha_{(1,0)(0,0)} = \alpha_{(1,-1)(0,0)} = \alpha_{(-1,0)(-1,0)} = \alpha_{(-1,-1)(-1,0)} = 1/12, \quad (\text{A.1b})$$

$$\alpha_{(0,0)(0,0)} = \alpha_{(0,0)(-1,0)} = \alpha_{(0,-1)(0,0)} = \alpha_{(0,-1)(-1,0)} = 1/24, \quad (\text{A.1c})$$

$$\alpha_{(1,0)(0,1)} = \alpha_{(1,-1)(0,-1)} = \alpha_{(-1,-1)(-1,-1)} = \alpha_{(-1,0)(-1,1)} = 1/24, \quad (\text{A.1d})$$

$$\beta_{(0,0)(1,0)} = \beta_{(1,-1)(0,-1)} = \beta_{(0,-1)(-1,-1)} = \beta_{(-1,0)(0,0)} = 1/24, \quad (\text{A.1e})$$

$$\gamma_{(0,1)(0,0)} = \gamma_{(0,0)(0,-1)} = \gamma_{(-1,-1)(-1,0)} = \gamma_{(-1,0)(-1,1)} = 1/24. \quad (\text{A.1f})$$

All other coefficients are equal to zero.

References

- [1] Vallis, G.K.. Atmospheric and Oceanic Fluid Dynamics. Cambridge, U.K., New York, U.S.A.: Cambridge University Press; 2006.
- [2] Salmon, R.. Lectures on Geophysical Fluid Dynamics. Oxford University Press, USA; 1998.
- [3] Muller, P.. Ertel’s potential vorticity theorem in physical oceanography. *Rev Geophys* 1995;33:67–97.
- [4] Eckart, C.. Variation principles of hydrodynamics. *Phys Fluids* 1960;3:421–427.
- [5] Phillips, N.A.. The equations of motion for a shallow rotating atmosphere and the traditional approximation. *J Atmos Sci* 1966;23:626–628.
- [6] Gerkema, T., Zimmerman, J.T.F., Maas, L.R.M., van Haren, H.. Geophysical and astrophysical fluid dynamics beyond the traditional approximation. *Rev Geophys* 2008;46:RG2004.

- [7] van Haren, H., Millot, C.. Gyroscopic waves in the Mediterranean Sea. *Geophys Res Lett* 2005;32:L24614.
- [8] van Haren, H.. Sharp near-equatorial transitions in inertial motions and deep-ocean step-formation. *Geophys Res Lett* 2005;32:Art. No. L01605.
- [9] Gerkema, T., Shrira, V.I.. Near-inertial waves in the ocean: beyond the “traditional approximation”. *J Fluid Mech* 2005;529:195–219.
- [10] Gerkema, T., Shrira, V.I.. Near-inertial waves on the non-traditional β -plane. *J Geophys Res* 2005;110:C10003.
- [11] Gerkema, T., Shrira, V.I.. Non-traditional reflection of internal waves from a sloping bottom, and the likelihood of critical reflection. *Geophys Res Lett* 2006;33:L06611.
- [12] Stewart, A.L., Dellar, P.J.. Multilayer shallow water equations with complete Coriolis force. Part 2. Linear plane waves. *J Fluid Mech* 2012;690:16–50.
- [13] Hua, B.L., Moore, D.W., Le Gentil, S.. Inertial nonlinear equilibration of equatorial flows. *J Fluid Mech* 1997;331:345–371.
- [14] Colin de Verdière, A.. The stability of short symmetric internal waves on sloping fronts: Beyond the traditional approximation. *J Phys Oceanogr* 2012;42:459–475.
- [15] Leibovich, S., Lele, S.K.. The influence of the horizontal component of Earth’s angular velocity on the instability of the Ekman layer. *J Fluid Mech* 1985;150:41–87.
- [16] Marshall, J., Schott, F.. Open-ocean convection: Observations, theory, and models. *Rev Geophys* 1999;37:1–64.
- [17] Stewart, A.L., Dellar, P.J.. Multilayer shallow water equations with complete coriolis force. Part 3. Hyperbolicity and stability under shear. *J Fluid Mech* 2013;723:289–317.
- [18] Stewart, A.L., Dellar, P.J.. The rôle of the complete Coriolis force in cross-equatorial flow of abyssal ocean currents. *Ocean Model* 2011;38:187–202.
- [19] Stewart, A.L., Dellar, P.J.. Cross-equatorial flow through an abyssal channel under the complete Coriolis force: Two-dimensional solutions. *Ocean Model* 2011;40:87–104.
- [20] Stewart, A.L., Dellar, P.J.. Cross-equatorial channel flow with zero potential vorticity under the complete Coriolis force. *IMA J Appl Math* 2012;77:626–651.
- [21] Müller, R.. A note on the relation between the “traditional approximation” and the metric of the primitive equations. *Tellus A* 1989;41A:175–178.
- [22] White, A.A., Bromley, R.A.. Dynamically consistent, quasi-hydrostatic equations for global models with a complete representation of the Coriolis force. *Q J Roy Meteor Soc* 1995;121:399–418.
- [23] White, A.A.. A view of the equations of meteorological dynamics and various approximations. In: Norbury, J., Roulstone, I., editors. *Large-Scale Atmosphere-Ocean Dynamics 1: Analytical Methods and Numerical Models*. Cambridge: Cambridge University Press; 2002, p. 1–100.
- [24] White, A.A., Hoskins, B.J., Roulstone, I., Staniforth, A.. Consistent approximate models of the global atmosphere: shallow, deep, hydrostatic, quasi-hydrostatic and non-hydrostatic. *Q J Roy Meteor Soc* 2005;131:2081–2107.
- [25] Tort, M., Dubos, T.. Dynamically consistent shallow-atmosphere equations with a complete Coriolis force. *Q J Roy Meteor Soc* 2014;140(684):2388–2392.
- [26] Tort, M., Dubos, T.. Usual approximations to the equations of atmospheric motion: A variational perspective. *J Atmos Sci* 2014;71(7):2452–2466.
- [27] Dellar, P.J., Salmon, R.. Shallow water equations with a complete Coriolis force and topography. *Phys Fluids* 2005;17:106601–19.
- [28] Stewart, A.L., Dellar, P.J.. Multilayer shallow water equations with complete Coriolis force. Part 1. Derivation on a non-traditional beta-plane. *J Fluid Mech* 2010;651:387–413.
- [29] Ledwell, J.R., Watson, A.J., Law, C.S.. Evidence for slow mixing across the pycnocline from an open-ocean tracer-release experiment. *Nature* 1993;364(6439):701–703.
- [30] Roberts, M., Marshall, D.. Do we require adiabatic dissipation schemes in eddy-resolving ocean models? *J Phys Oceanogr* 1998;28(10):2050–2063.
- [31] Bleck, R., Rooth, C., Hu, D., Smith, L.T.. Salinity-driven thermocline transients in a wind- and thermohaline-forced isopycnal coordinate model of the North Atlantic. *J Phys Oceanogr* 1992;22:1486–1505.
- [32] Bleck, R., Chassignet, E.. Simulating the oceanic circulation with isopycnal-coordinate models. In: Majumdar, S., Miller, E., Forbe, G., Schmalz, R., Panah, A., editors. *The Oceans: Physical-Chemical Dynamics and Human Impact*. Easton, PA: Pennsylvania Acad. Sci.; 1994, p. 17–39.
- [33] Hallberg, R., Rhines, P.. Buoyancy-driven circulation in an ocean basin with isopycnals intersecting the sloping boundary. *J Phys Oceanogr* 1996;26:913–940.
- [34] Vitousek, S., Fringer, O.B.. A nonhydrostatic, isopycnal-coordinate ocean model for internal waves. *Ocean Model* 2014;83:118–144.
- [35] Frank, J., Gottwald, G., Reich, S.. A Hamiltonian particle-mesh method for the rotating shallow water equations. In: Griebel, M., Schweitzer, M.A., editors. *Meshfree Methods for Partial Differential Equations*; vol. 26 of *Lecture Notes in Computational Science and Engineering*. Springer; 2002, p. 131–142.
- [36] Dritschel, D.G., Polvani, L.M., Mohebalhojeh, A.R.. The contour-advective semi-Lagrangian algorithm for the shallow water equations. *Mon Weather Rev* 1999;127:1551–1565.
- [37] Thompson, P.D.. On the structure of the hydrodynamical equations for two-dimensional flows of an incompressible fluid: The role of integral invariance. In: Tabor, M., Treve, Y.M., editors. *Mathematical Methods in Hydrodynamics and Integrability of Dynamical Systems*; vol. 88 of *AIP Conference Proceedings*. New York: American Institute of Physics; 1982, p. 301–317.
- [38] Arakawa, A.. Computational design for long-term numerical integration of the equations of fluid motion: Two-dimensional

- incompressible flow. Part I. *J Comput Phys* 1966;1:119–143.
- [39] Arakawa, A., Lamb, V.R.. Computational design of the basic dynamical processes of the ucla general circulation model. In: Chang, J., editor. *General Circulation Models of the Atmosphere*; vol. 17 of *Methods in Computational Physics*. San Francisco: Academic Press; 1977, p. 173–265.
- [40] Thuburn, J., Kent, J., Wood, N.. Cascades, backscatter and conservation in numerical models of two-dimensional turbulence. *Q J Roy Met Soc* 2014;140(679):626–638.
- [41] Fornberg, B.. On the instability of leap-frog and Crank–Nicolson approximations of a nonlinear partial differential equation. *Math Comput* 1973;27:45–57.
- [42] Arakawa, A., Lamb, V.R.. A potential enstrophy and energy conserving scheme for the shallow water equations. *Mon Weather Rev* 1981;109:18–36.
- [43] Hollingsworth, A., Källberg, P., Renner, V., Burridge, D.M.. An internal symmetric computational instability. *Q J Roy Meteor Soc* 1983;109:417–428.
- [44] Takano, K., Wurtele, M.G.. A fourth-order energy and potential enstrophy conserving difference scheme. Tech. Rep. AFGL-TR-82-0205; Air Force Geophysics Laboratory, Hanscom Air Force Base, Bedford, MA; 1982.
- [45] Abramopoulos, F.. Generalized energy and potential enstrophy conserving finite difference schemes for the shallow water equations. *Mon Weather Rev* 1988;116(3):650–662.
- [46] Abramopoulos, F.. A new fourth-order enstrophy and energy conserving scheme. *Mon Weather Rev* 1991;119(1):128–133.
- [47] Salmon, R.. Poisson-bracket approach to the construction of energy- and potential-enstrophy-conserving algorithms for the shallow-water equations. *J Atmos Sci* 2004;61:2016–2036.
- [48] Ringler, T.D., Randall, D.A.. A potential enstrophy and energy conserving numerical scheme for solution of the shallow-water equations on a geodesic grid. *Mon Weather Rev* 2002;130:1397–1410.
- [49] McRae, A.T.T., Cotter, C.J.. Energy- and enstrophy-conserving schemes for the shallow-water equations, based on mimetic finite elements. *Q J Roy Meteor Soc* 2014;140:2223–2234.
- [50] Salmon, R.. Hamiltonian fluid mechanics. *Annu Rev Fluid Mech* 1988;20:225–256.
- [51] Shepherd, T.G.. Symmetries, conservation laws, and Hamiltonian structure in geophysical fluid dynamics. *Adv Geophys* 1990;32:287–338.
- [52] Morrison, P.J.. Hamiltonian description of the ideal fluid. *Rev Mod Phys* 1998;70:467–521.
- [53] Durran, D.R.. The third-order Adams-Bashforth method: an attractive alternative to leapfrog time-differencing. *Mon Weather Rev* 1991;119:702–720.
- [54] Tort, M., Dubos, T., Melvin, T.. Energy-conserving finite-difference schemes for quasi-hydrostatic equations. *Q J Roy Meteor Soc* 2015;.
- [55] Salmon, R.. A general method for conserving quantities related to potential vorticity. *Nonlinearity* 2005;18:R1–R16.
- [56] Salmon, R.. A general method for conserving energy and potential enstrophy in shallow-water models. *J Atmos Sci* 2007;64:515–531.
- [57] Arakawa, A., Hsu, Y.J.G.. Energy conserving and potential-enstrophy dissipating schemes for the shallow water equations. *Mon Weather Rev* 1990;118:1960–1969.
- [58] Dellar, P.J.. Variations on a beta-plane: derivation of non-traditional beta-plane equations from Hamilton’s principle on a sphere. *J Fluid Mech* 2011;674:174–195.
- [59] Ripa, P.. Symmetries and conservation laws for internal gravity waves. In: West, B.J., editor. *Nonlinear Properties of Internal Waves*; vol. 76 of *AIP Conference Proceedings*. New York: American Institute of Physics; 1981, p. 281–306.
- [60] Salmon, R.. Hamilton’s principle and Ertel’s theorem. In: Tabor, M., Treve, Y.M., editors. *Mathematical Methods in Hydrodynamics and Integrability of Dynamical Systems*; vol. 88 of *AIP Conference Proceedings*. New York: American Institute of Physics; 1982, p. 127–135.
- [61] Hou, T.Y., Li, R.. Computing nearly singular solutions using pseudo-spectral methods. *J Comput Phys* 2007;226:379–397.
- [62] Engquist, B., Sjögreen, B.. The convergence rate of finite difference schemes in the presence of shocks. *SIAM J Numer Anal* 1998;35:2464–2485.
- [63] Polvani, L.M., McWilliams, J.C., Spall, M.A., Ford, R.. The coherent structures of shallow-water turbulence: Deformation-radius effects, cyclone/anticyclone asymmetry and gravity-wave generation. *Chaos* 1994;4:177–186.
- [64] Kahan, W.. Further remarks on reducing truncation errors. *Commun ACM* 1965;8:40.
- [65] Higham, N.. *Accuracy and Stability of Numerical Algorithms*. Society for Industrial and Applied Mathematics; second ed.; 2002.
- [66] Ketefian, G., Jacobson, M.. A mass, energy, vorticity, and potential enstrophy conserving lateral fluid-land boundary scheme for the shallow water equations. *J Comput Phys* 2009;228:1–32.
- [67] Ketefian, G., Jacobson, M.. A mass, energy, vorticity, and potential enstrophy conserving lateral boundary scheme for the shallow water equations using piecewise linear boundary approximations. *J Comput Phys* 2011;230:2751–2793.
- [68] Salmon, R.. An ocean circulation model based on operator-splitting, Hamiltonian brackets, and the inclusion of sound waves. *J Phys Oceanogr* 2009;39:1615–1633.
- [69] Grimshaw, R.H.J.. A note on the β -plane approximation. *Tellus A* 1975;27:351–357.
- [70] Richards, A.. University of Oxford Advanced Research Computing. Zenodo document doi:10.5281/zenodo.22558; 2015.